

Causally constrained reduced-order neural models of complex turbulent dynamical systems

Fabrizio Falasca* and Laure Zanna
*Courant Institute School of Mathematics,
 Computing and Data Science
 New York University, New York, NY, USA*

We introduce a flexible framework based on response theory and score matching to suppress spurious, noncausal dependencies in reduced-order neural emulators of turbulent systems, focusing on climate dynamics as a proof-of-concept. We showcase the approach using the stochastic Charney–DeVore model as a relevant prototype for low-frequency atmospheric variability. We show that the resulting causal constraints enhance neural emulators’ ability to respond to both weak and strong external forcings, despite being trained exclusively on unforced data. The approach is broadly applicable to modeling complex turbulent dynamical systems in reduced spaces and can be readily integrated into general neural network architectures.

I. INTRODUCTION

Modeling and understanding complex turbulent dynamical systems often requires abandoning full microscopic descriptions in favor of reduced-order models, where coarse-grained variables evolve according to effective stochastic dynamics [1, 2]. Such reduced stochastic descriptions are fundamental across physics, ranging from chemical physics [3, 4], neuroscience [5, 6], mathematical physics [7, 8], turbulence [9, 10], climate science [11–17], and many others. In practice, one is often faced with an inverse problem: given long trajectories of a Markovian, coarse-grained system, construct a data-driven model that faithfully reproduces its statistical and dynamical features [18–31]. Recent advances in machine learning further contribute to inverse modeling by providing flexible neural network architectures for data-driven emulation, with promising applications in fluid dynamics [32–34], weather [35, 36], and climate science [37–41]. However, neural network-based models are typically agnostic to the underlying physics, which can lead to non-physical behavior, such as violations of energy conservation - an issue that can be addressed through appropriate constraints [21, 23, 42, 43] - or incorrect responses to external forcings. The latter issue has been documented in neural weather models [44] and, especially, in climate emulators [45, 46]. This limitation highlights a central open challenge for neural emulators of physical systems: high skill in reproducing stationary statistics does not guarantee accurate responses to external perturbations, thereby limiting the use of such models for process understanding through sensitivity analysis and the exploration of “what if?” scenarios. Crucially, a model’s ability to respond to forcings is inherently linked to causality, since cause–effect relationships in physical systems are inferred through external interventions [47–50], commonly realized via perturbation–response experiments (see [51, 52] in the contexts of neuroscience and climate,

respectively). This connection suggests that constraining a data-driven model to respect a given “correct” causal structure should improve its ability to respond to external forcings. The resulting challenge is twofold: to infer causal relationships from stationary, unperturbed data alone, and to incorporate this information into neural emulators, all within a computationally efficient framework that is both scalable and practical. In this context, the Fluctuation–Dissipation Theorem (FDT) plays a fundamental role as it provides a bridge between forced and natural fluctuations of physical systems [53–58]. The work of Baldovin et al. (2020) [59] showed that the FDT provides a rigorous causal inference strategy in the interventional sense directly from data, and this approach has since been adopted in a growing body of work [28, 31, 60–65]. In this Letter, we take this line of research one step further by leveraging the FDT to constrain the training of general neural emulators of physical systems. Given a trajectory $\mathbf{x}(t) = [x_1, x_2, \dots, x_n](t)$ of a multivariate Markovian system, our framework proceeds in two steps: (i) use the FDT to infer the direct causal couplings $x_j \rightarrow x_k$ across degrees of freedom x_j, x_k ; (ii) learn a stochastic neural model from $\mathbf{x}(t)$ while preserving the inferred causal structure. A related direction was recently proposed by Chen and Liu (2025) [27], who used causation entropy to rank candidate functions in the construction of causally constrained reduced-order models, highlighting the benefits of causally informed approaches. Our work addresses a complementary setting by providing a practical strategy to enforce a prescribed causal structure within general neural network architectures. To illustrate the methodology, we focus on climate dynamics as a representative example of a complex, turbulent dynamical system that is necessarily modeled through an effective, coarse-grained description [9, 13, 23], and for which accurate modeling of forced responses is essential [31]. We consider a stochastic version of the Charney–DeVore model [66], relevant for conceptual studies of low-frequency climate variability. This choice provides a simplified testbed that nevertheless retains key features of realistic coarse-grained climate dynamics, in-

* fabri.falasca@nyu.edu

cluding strong mixing, fast decay of autocorrelations, and regular, unimodal distributions [67, 68]. We show that causally constrained neural emulators substantially improve the ability of neural networks to capture responses to both weak and strong forcings. In particular, the causal emulator accurately reproduces responses beyond the linear regime, including time-dependent shifts of the attractor in state space, despite being trained solely on stationary, unperturbed data.

II. FRAMEWORK: FROM LINEAR RESPONSE TO CAUSAL CONSTRAINTS

a. Fluctuation–Dissipation Theorem (FDT) and causality Given an n -dimensional stochastic nonlinear system $\mathbf{x}(t)$, the FDT [55, 56] states that the linear response, in the ensemble average sense, of a degree of freedom $x_k(t)$ to an infinitesimally small impulse perturbation $\delta x_j(0)$ applied to component $x_j(0)$ can be written as:

$$R_{k,j}(t) = \frac{\delta \langle x_k(t) \rangle}{\delta x_j(0)} = -\langle x_k(t) s_j(\mathbf{x}(0)) \rangle, \quad (1)$$

$$s(\mathbf{x}) = \nabla \log \rho(\mathbf{x}).$$

$\rho(\mathbf{x})$ is the system’s invariant density and $s(\mathbf{x})$ is the *score function* of the system [65, 69]. The focus on stochastic systems allows us to circumvent difficulties with deterministic dissipative dynamical systems, where the invariant measure is singular [70–72]. The brackets $\langle \cdot \rangle$ represents ensemble averages, computed over the invariant density. Eq. (1) provides a rigorous strategy for inferring causal relations in physical systems in the interventional sense from data alone [59]. As discussed in [31], $R_{k,j}(t)$ supports multiple causal interpretations: values at the shortest time scale ($t = dt$) encode direct causal links $x_j \rightarrow x_k$. Nonzero responses at later times reflect indirect causal links. Additionally, a cumulative measure of causal influence can be defined as $D_{k,j} = \int_0^\infty R_{k,j}(t) dt$ [59]. The causal constraints proposed in this work focus on the direct causal links, $R_{k,j}(dt)$. In practice the response is computed for standardized data as $(\sigma_j/\sigma_k) R_{k,j}(dt)$, σ_i representing the standard deviation of x_i ; for simplicity, we denote this standardized operator by $R_{k,j}$.

b. FDT from data The main challenge in estimating responses via Eq. (1) lies in estimating the score function $s(\mathbf{x})$, particularly in high-dimensional settings. Traditional studies have adopted the quasi-Gaussian (qG, hereafter) ansatz [55, 73], in which ρ is approximated by a Gaussian. The qG approximation has proven effective for predicting mean responses, even for nonlinear problems [55, 57, 65, 67]. Recent developments in score-based generative modeling [74, 75], offer new ways forward to overcome previous approximations by parametrizing the score function directly from data. Importantly, when provided with enough data, these new strategies scale to high-dimensional systems such as quasi-geostrophic flows [76], idealized ocean flows [77], weather [78], climate

[79], fluid dynamics [80], among others. The estimated score $s(\mathbf{x})$ can then be inserted into the analytical response formula in Eq. (1), circumventing the need for explicit approximations of the invariant density, as in the quasi-Gaussian case. This approach was first proposed in [69]. These advances are leading to a set of score-estimation techniques rather than a single strategy. For example, [65] highlighted different denoising score-matching procedures tailored to the dimensionality of the underlying system. Here, we further contribute to this “FDT–generative modeling toolbox”. Specifically, we adopt the score-matching estimator proposed in [81], allowing us to infer the score directly on the attractor, rather than up to a small noise perturbation (e.g., as in denoising score matching). The estimated score is used as an initial approximation and is then refined using the correction procedure introduced in [69]. Details are reported in Section I of the Supplemental Material.

c. Causal constraints. Consider a stochastic dynamical system

$$\dot{x}_i(t) = f_i(x_1, x_2, \dots, x_n) + \sigma_i \xi_i(t), \quad \text{with } i = 1, 2, \dots, n,$$

where $\sigma_i \xi_i(t)$ is a stochastic forcing, $\xi(t)$ being a standard Gaussian white noise process. A perturbation to x_j can affect x_k at the next time step only if f_k depends on x_j . Thus, in the limit $dt \rightarrow 0$, $\partial f_k / \partial x_j \equiv 0$ implies the *absence* of a direct causal link and consequently, a vanishing short-time response $R_{k,j}(dt) = 0$. In practice, the system’s Jacobian is not observable from data, and a reliable numerical estimation is unfeasible in high-dimensional systems. However, the short-time response $R_{k,j}(dt)$ can be efficiently estimated from unperturbed data using the FDT in Eq. (1) as shown in [65]. A vanishing response at the shortest resolved time scale thus implies $\langle \partial f_k(\mathbf{x}) / \partial x_j \rangle = 0$ for $j \neq k$. This information on vanishing entries of the ensemble-averaged Jacobian is used to constrain neural architectures. Thus, given a long trajectory of $\mathbf{x}(t)$, we first estimate the response operator $\mathbf{R}(dt) \in \mathbb{R}^{n,n}$ with the score-matching procedure introduced earlier. We then proceed by constructing a binary adjacency matrix $\mathbf{A} \in \mathbb{R}^{n,n}$, by thresholding $\mathbf{R}(dt)$. $A_{k,j} = 0$ denoting the absence of a direct causal link $x_j \rightarrow x_k$, and $A_{k,j} = 1$ denoting its presence. One way to threshold $R_{k,j}(dt)$ is to examine its values on a logarithmic scale; a visual inspection of the response magnitudes often reveals a clear separation between significant links and noise. The absence of such separation may itself be informative, suggesting a densely connected system, in which case no additional causal constraints are needed. To provide an unsupervised criterion, we propose the following procedure:

i. *Self-interactions.* We assume that for any dissipative dynamical system $x_j \rightarrow x_j$ and therefore $A_{j,j} = 1$.

ii. *Cross-interactions.* We consider the off-diagonal values of $R_{k,j}(dt), j \neq k$, and apply a logarithmic transformation $\ln |R_{k,j}(dt)|$. This helps separate potential causal links (larger responses) from

the bulk of spurious, near-zero interactions. A k -means algorithm [82] ($k = 2$) is then used to partition these log-scaled values into two clusters, corresponding to “significant” and “insignificant” responses. An entry of $A_{k,j} = 1$ is set if its corresponding $\ln|R_{k,j}(dt)|$ value belongs to the cluster with the larger centroid; otherwise, it is set to 0.

The causal Adjacency matrix is then used to constrain the training of a neural emulator. Given a n -dimensional trajectory $\mathbf{x}(t) = [x_1, x_2, \dots, x_n](t)$ we fit a neural operator \mathbf{f} such that $\dot{\mathbf{x}}(t) = \mathbf{f}(\mathbf{x}) + \boldsymbol{\Sigma}\xi(t)$. The causal constraints are imposed on the deterministic drift \mathbf{f} . We learn \mathbf{f} via a mean squared error (MSE) minimization such that $\Delta\mathbf{x} = \mathbf{x}(t+1) - \mathbf{x}(t) = \mathbf{f}(\mathbf{x}(t))$, where the time unit has been rescaled by the time sampling interval. Details on the learning process are found in the SM, Section III. A “vanilla”, unconstrained operator \mathbf{f} is trained by minimizing MSE as $\mathcal{L} = \text{MSE}(\Delta\mathbf{x}, \mathbf{f}(\mathbf{x}))$. The causally constrained emulator is trained by minimizing the following loss function:

$$\mathcal{L} = \text{MSE}(\Delta\mathbf{x}, \mathbf{f}(\mathbf{x}(t))) + \lambda \sum_{k,j \in \mathcal{S}} \left(\frac{\partial f_k}{\partial x_j} \right)^2, \quad (2)$$

where \mathcal{S} is the set of pairs (k, j) for which the causal adjacency matrix $A_{k,j} = 0$. λ is a parameter determining the strength of the regularization. The derivatives are obtained via automatic differentiation [83]. We adopt soft constraints for two main reasons. First, they are computationally efficient [43]. Second, in real-world, high-dimensional climate systems with partial observations and finite data, causal estimates are inherently uncertain. In this regime, hard constraints based on imperfect causal information will introduce biases into the learned dynamics. Soft constraints, in contrast, provide a flexible form of regularization, ensuring an appropriate balance between data fidelity, as captured by the MSE, and causal regularization. Additionally, we note that the regularization in Eq. (10) can be adapted to novel architectures, including generative models [84], which we leave to future work.

Possible limitations for idealized systems. The proposed constraints leverage information about zeros of the *ensemble-averaged* Jacobian to constrain the state-dependent Jacobian. While this choice is practical and efficient, it can be limiting in idealized systems, for example because of *exact* symmetries. In such cases, nonzero local couplings may cancel in ensemble averages, yielding $\langle \partial f_k(\mathbf{x}) / \partial x_j \rangle = 0$ even if $\partial f_k(\mathbf{x}) / \partial x_j \neq 0$, as occurs, for example, in the Lorenz '63 model [85]. In such idealized settings, applying the proposed approach may require a symmetry-reduction step, as advocated in [86] and demonstrated in [87] for the Lorenz '63 system. These limitations are not restrictive for realistic turbulent system considered here, such as weather and climate, which lack exact symmetries, are only partially observed, and admit multiple effective coarse-grained representations. In this regime, dominant interactions among coarse-grained variables are often well approximated by

a *state-independent* linear operator, with nonlinearities providing higher-order corrections [13, 18, 55, 88–92]. There is no unique law to be discovered, instead the learned drift \mathbf{f} represents one admissible effective realization, regularized to ensure physically consistent response behavior and agreement with observed statistics. Further details are provided in Section II of the SM.

Practical assessment of causal constraints from data alone. Finally, the utility of causal constraints for a given system can be readily assessed by fitting a constrained model and an unconstrained counterpart. A key diagnostic is the comparison of the response operator computed from the emulators (see Section V of the SM) with the FDT-based operator in Eq. (1). When the inferred causal structure is informative, the constrained emulator improves the representation of linear responses without degrading the representation of stationary statistics. Moreover, comparing modeled and FDT-inferred response operators provides a natural criterion for *a posteriori* calibration of neural emulators based on forced responses. Related response-based calibration ideas have been explored in previous studies [93, 94]; a systematic formulation tailored to neural emulators and causal constraints is left for future work.

III. CAUSAL CONSTRAINTS IN PRACTICE

Test-model for low-frequency climate variability. To showcase the framework, we consider a stochastic version of the Charney–DeVore model [66], “CdV” hereafter. The model was obtained as a six-dimensional Galerkin truncation of the barotropic vorticity equation on a β -plane channel with topography. The formulation considered here is the one further proposed by De Swart [95]. The model has been widely studied in the context of large-scale atmospheric circulation [96–98], as well as in computational studies of regime transitions and rare events [99]. The model takes the following form:

$$\begin{aligned} \dot{x}_1 &= \tilde{\gamma}_1 x_3 - C(x_1 - x_1^*) + \sigma \xi_1(t), \\ \dot{x}_2 &= -(\alpha_1 x_1 - \beta_1) x_3 - C x_2 - \delta_1 x_4 x_6 + \sigma \xi_2(t), \\ \dot{x}_3 &= (\alpha_1 x_1 - \beta_1) x_2 - \gamma_1 x_1 - C x_3 + \delta_1 x_4 x_5 + \sigma \xi_3(t), \\ \dot{x}_4 &= \tilde{\gamma}_2 x_6 - C(x_4 - x_4^*) + \varepsilon(x_2 x_6 - x_3 x_5) + \sigma \xi_4(t), \\ \dot{x}_5 &= -(\alpha_2 x_1 - \beta_2) x_6 - C x_5 - \delta_2 x_4 x_3 + \sigma \xi_5(t), \\ \dot{x}_6 &= (\alpha_2 x_1 - \beta_2) x_5 - \gamma_2 x_4 - C x_6 + \delta_2 x_4 x_2 + \sigma \xi_6(t). \end{aligned} \quad (3)$$

In what follows, the six variables x_i serve as an effective reduced-order description of an underlying high-dimensional dynamical system, from which we aim to learn a causally constrained neural emulator. The parameters and their physical interpretation are reported in Section IV of the SM. $\xi_i(t), i = 1, \dots, 6$ is a Gaussian white noise with zero mean, unit variance, and σ is the noise amplitude. This stochastic forcing mimics the effect of unresolved fast processes. The model is an ideal first test case for our framework of large-scale, low-frequency

climate dynamics for two main reasons. First, Eq. (3) features the abstract form $\dot{\mathbf{x}} = \mathbf{F} + \mathbf{Lx} + \mathbf{B}(\mathbf{x}, \mathbf{x}) + \Sigma \xi(t)$, with energy conserving quadratic nonlinearities such that $\mathbf{x} \cdot \mathbf{B}(\mathbf{x}, \mathbf{x}) = 0$; a structure that naturally arises when geophysical turbulent flows are projected onto orthogonal bases [9, 12, 55, 100]. Second, this system is strongly mixing, with fast decay of autocorrelations and regular, unimodal probability distributions: such properties are relevant for coarse-grained climate dynamics as found both in models and observational data [68, 101–103], and underlie the reduced-order modeling of realistic, complex turbulent systems [2]. In this respect, the resulting dynamics differ qualitatively from those of prototypical chaotic models like the Lorenz '63 system [85], which is weakly mixing, possesses exact symmetries, and exhibits a singular invariant measure [68].

We simulate this model for $T = 5 \cdot 10^7$ time-steps at $dt = 0.01$, i.e. $5 \cdot 10^5$ Model Time Units (MTU). This long integration serves as a stationary run to (i) infer the response operators $R_{k,j}(t)$ from data alone and (ii) to build neural emulators. Two emulators, with and without causal constraints, are then compared in terms of their ability to reproduce both stationary and perturbed statistics. While a comprehensive analysis is provided in the Supplemental Material, the main text highlights the identification of causal links and the ability of the causally constrained emulator to capture time-dependent responses in ensemble mean and variance under strong forcings.

a. Causal Adjacency matrix from data. Given a long trajectory $\mathbf{x}(t) = [x_1, \dots, x_6](t)$ of the CdV model, we infer the direct causal links through the steps proposed in the previous Section. The strategy is highlighted step by step in Figure 1. We infer the response operator at the shortest time scale $R_{k,j}(dt) = -\langle x_k(dt) s_j(\mathbf{x}(0)) \rangle$ via score-matching, consider only the off-diagonal elements, and apply the transformation $\ln |R_{k,j}(dt)|$; see Figure 1(a). We then apply a k -means algorithm ($k = 2$) to split the large responses from the spurious non-causal ones; see Figure 1(b). This information is used to define the Adjacency matrix in Figure 1(c), thus defining the causal functional form of the system to be imposed in the neural emulator; see 1(d). In Section VII of the SM we also report results for the inference of the response operator $R_{k,j}(t)$ over multiple time lags t using both the score-matching and quasi-Gaussian approximations, further illustrating the advantages of the score-matching approach.

b. Neural emulators. We learn two stochastic neural models from the long trajectory $\mathbf{x}(t) = [x_1, \dots, x_6](t)$ of the CdV model: one with causal constraints and one without. The latter referred to as “vanilla” emulator. The causally constrained emulator leverages the Adjacency matrix $A_{k,j}$ inferred in Figure 1(c) to suppress spurious, non-causal terms through the new loss function in Eq. (10). The set \mathcal{S} of pairs (k, j) to be used in Eq. (10) is given by the zeros of $A_{k,j}$ in Figure 1(c) and equal to $\mathcal{S} =$

$\{(1, 2), (1, 4), (1, 5), (1, 6), (2, 5), (3, 6), (4, 1), (5, 2), (6, 3)\}$. Both neural emulators have been trained with the same hyper-parameters, the only difference being the addition of the regularization term as in Eq. (10) for the causally constrained model.

c. Stationary statistics. Given the two emulators defined above, we simulate a long trajectory of $T = 10^7$ time steps. We then examine two stationary statistics: the invariant probability distribution (PDF) and the autocorrelation functions (ACFs). The analysis is reported in Section VI of the SM: both the vanilla and the causally constrained emulator reproduce these stationary statistics well.

d. Perturbed statistics: linear regime. We assess the ability of the emulators to reproduce perturbed statistics in the linear-response regime by analyzing the impulse response operator for the ensemble mean and variance, following [31]. A small impulse perturbation $\delta x_j(0)$ is applied at $t = 0$, and the response of observables $A(x_k(t)) = x_k(t)$ (mean) and $A(x_k(t)) = (x_k(t) - \mu_k(t))^2$ (variance) is measured, $\mu(t)$ representing the time-dependent mean. Here, we perturb $x_1(0)$ and report the self-response of $x_1(t)$ in mean and variance (Fig. 2). The vanilla emulator reproduces the response operator accurately, as expected given the large training dataset and Markovianity of the system [31]. However, the causally constrained emulator yields a systematically improved representation of both mean and variance responses. This improvement persists for the full response operator $R_{k,j}(t)$ across all variables (see Figures 4–5 of the Supplemental Material). A quantitative summary of this improvement is provided by the total time-dependent MSE, aggregated over all j and k , between the emulators and the ground truth, reported in Figure 6 of the SM.

e. Perturbed statistics: nonlinear regime. We now probe the nonlinear response regime by applying a large step forcing \mathbf{F} to both the numerical model and the neural emulators. As in the linear response analysis, the forcing is applied to x_1 . The forced dynamics are given by $\dot{\mathbf{x}} = \mathbf{F} + \mathbf{f}(\mathbf{x}) + \Sigma \xi(t)$, where $\mathbf{F} = (\sigma_1, 0, 0, 0, 0, 0)$ for $t \geq 0$, σ_1 being the std. dev. of the x_1 variable. The forcing amplitude is intentionally set very high to induce a strongly nonlinear response. We simulate an ensemble of 10^5 forced realizations and measure the time-dependent response of the ensemble mean and variance relative to the unperturbed stationary distribution. The forcing alters the system’s attractor through time-dependent feedbacks across degrees of freedom. Figure 3 shows the resulting self-response of the marginal distribution of $x_1(t)$; responses of the full system are reported in Figures 7–8 of the Supplemental Material. The numerical model exhibits a pronounced transient response, relaxing toward a new equilibrium after approximately 40 model time units. Therefore, the external forcing modifies the characteristics of the attractor in state space. The causally constrained emulator accurately reproduces these nonlinear forced responses, particularly in the ensemble mean. By contrast, the vanilla emulator becomes unstable after a

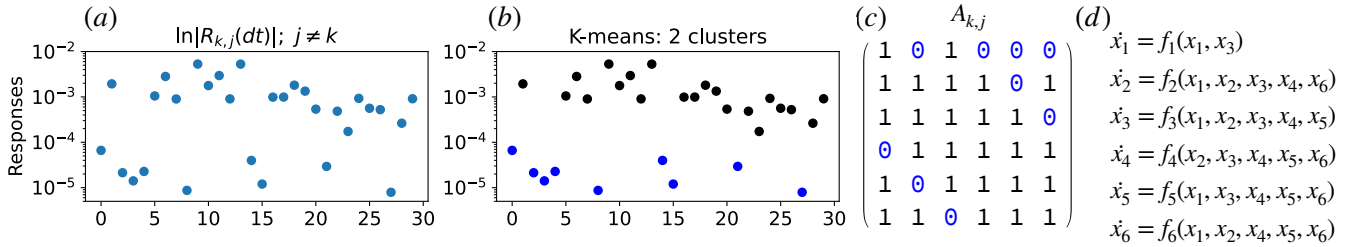


FIG. 1: Causal constraining of the CdV model (Eq. (3)) from data through the FDT. Panel (a): The 30 off-diagonal responses $\ln|R_{k,j}(dt)|$ (evaluated at the shortest time scale $t = dt$), flattened and plotted against a dummy index. Panel (b): Unsupervised identification of a response threshold via k -means clustering ($k = 2$): clusters are colored in black and blue. Panel (c): Causal adjacency matrix: $A_{k,j} = 1$ is assigned if its corresponding response value lies in the higher centroid cluster; otherwise $A_{k,j} = 0$. Panel (d): “causal” deterministic functional form to be enforced in the emulator loss function in Eq. (10).

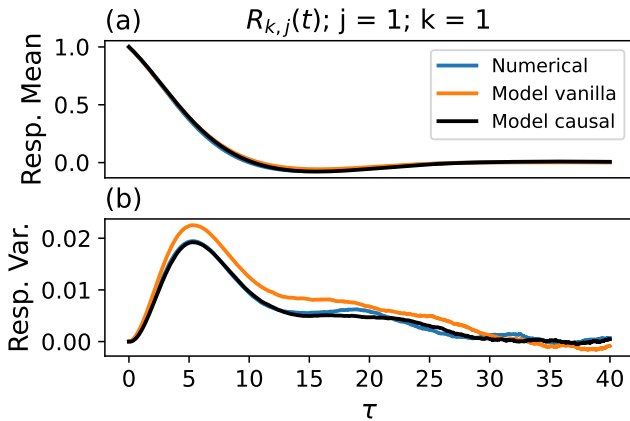


FIG. 2: Perturbed statistics: linear regime. Self-response operator of mean and variance for the variable x_1 . Panel (a): Time-dependent, response in ensemble mean of variable $x_1(t)$ to an impulse perturbation $\delta x_1(0)$ imposed on $x_1(0)$ at time $t = 0$. Formally: $R_{1,1}(t) = \delta\langle x_1(t) \rangle / \delta x_1(0)$. Panel (b) same as Panel (a) but for response in ensemble variance. Responses are computed using an ensemble of $N_e = 10^6$ members. The magnitude of the impulse perturbation is set to $10^{-1}\sigma_1$, σ_1 being the standard deviation of x_1 . Labels: “Numerical” (numerical model), Model vanilla” (vanilla, unconstrained, emulator), and “Model causal” (causally constrained emulator).

short transient under the same forcing. This behavior is robust: when large step forcings are applied to each degree of freedom, the vanilla emulator becomes unstable in three out of six cases, whereas the causally constrained emulator remains stable for all forcings (see Section VIII of the SM). In general, despite the large forcing amplitude, we observe that the causally constrained emulator provides a good approximation of the forced responses in both ensemble mean and variance.

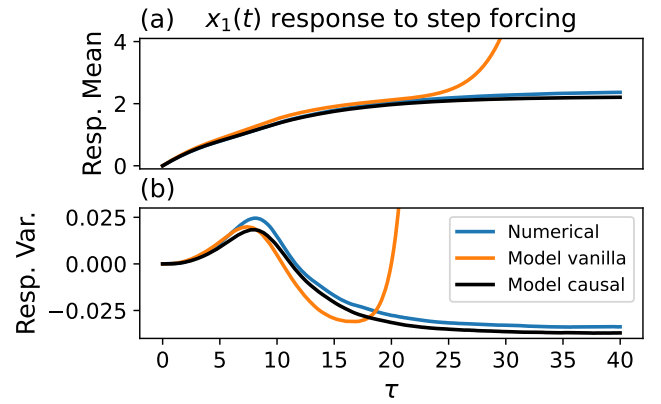


FIG. 3: Perturbed statistics: nonlinear regime. Time-dependent response of the ensemble mean and variance of x_1 to a strong step function forcing. Forcing: step function $\mathbf{F} = (\sigma_1, 0, 0, 0, 0, 0)$ for $t \geq 0$, applied on the right-hand side of the numerical model and emulators. σ_1 is the standard deviation of x_1 . Responses are computed using an ensemble of $N_e = 10^5$ members. Panel (a): response in ensemble mean. Panel (b): response in ensemble variance. Labels: “Numerical” (numerical model), “Model vanilla” (vanilla, unconstrained, emulator), and “Model causal” (causally constrained emulator).

IV. DISCUSSION AND CONCLUSIONS

We introduced a strategy that leverages the Fluctuation–Dissipation Theorem and score matching to (i) identify direct causal links from long trajectories of Markovian physical systems and (ii) impose this causal information as constraints in neural emulators. These constraints improve the ability of reduced-order neural emulators to capture responses to both weak and strong external perturbations, even if trained on unforced data alone. In practice, the choice of a Markovian, coarse-grained representation of an underlying

high-dimensional dynamical system is itself a central challenge, as emphasized in classical work [104] and revisited in recent studies [31, 50, 94]. However, given an appropriate choice of coarse-grained variables, the proposed constraints can be readily implemented in general neural network architectures. The framework is modular and can be combined with any data-driven estimator of the FDT operator, including recent proposals such as [58, 105], as well as with alternative causal discovery methods, for example [106]. A natural next step is to extend this framework to observational climate data and to develop causally consistent, reduced-order neural models of the global atmosphere and ocean, including within emerging probabilistic architectures such as stochastic interpolants [43, 84, 107]. This perspective also opens the possibility of combining causal constraints with complementary physical constraints, such as energy conservation [42], to jointly enforce stability and physical fidelity in neural emulators. Additionally, in realistic applications, data are often scarce and partially observed, leading to imperfect causal estimates. An important open direction is to assess how accurate such estimates must be - and whether approximate, quasi-Gaussian

FDT operators may already suffice [68] - to construct imperfect emulators that nevertheless exhibit skill in responding to external perturbations. Finally, while motivated by climate dynamics, the proposed strategy applies to neural modeling of general complex turbulent dynamical systems in reduced coordinate spaces. In such settings, causal constraints provide a practical and readily implementable addition to general neural network architectures.

Code availability Codes will be soon available at <https://github.com/FabriFalasca/Causally-constrained-neural-emulators/>

ACKNOWLEDGMENTS

This research was supported by Schmidt Sciences, LLC, through the M²LInES project. Computational resources and support were provided in part by the NYU IT High Performance Computing facilities, services, and staff. F.F. is grateful to Rory Basinski and Matthieu Blanke for many enriching discussions on this subject.

[1] P. Castiglione, M. Falcioni, A. Lesne, and A. Vulpiani, *Chaos and Coarse Graining in Statistical Mechanics* (Cambridge University Press, 2008).

[2] A. Majda, *Introduction to Turbulent Dynamical Systems in Complex Systems* (Springer Cham, 2016).

[3] S. Izvekov and G. Voth, Multiscale coarse graining of liquid-state systems, *J. Chem. Phys* **123**, <https://doi.org/10.1063/1.2038787> (2005).

[4] J.-H. Prinz, H. Wu, M. Sarich, B. Keller, M. Senne, M. Held, J. Chodera, C. Schütte, and F. Noé, Markov models of molecular kinetics: Generation and validation, *J. Chem. Phys* **134**, <https://doi.org/10.1063/1.3565032> (2011).

[5] L. Harrison, O. David, and K. Friston, Stochastic models of neuronal dynamics, *Phil. Trans. R. Soc. B* **360**, 1075–1091 (2005).

[6] A. Rangan, L. Tao, G. Kovacic, and D. Cai, Multiscale modeling of the primary visual cortex, *IEEE Eng Med Biol Mag.* **28**, 19 (2009).

[7] A. Roberts, Normal form transforms separate slow and fast modes in stochastic dynamical systems, *Physica A: Statistical Mechanics and its Applications* **387**, 12 (2008).

[8] A. J. Roberts, Resolving the multitude of microscale interactions accurately models stochastic partial differential equations, *LMS Journal of Computation and Mathematics* **9**, 193–221 (2006).

[9] A. Majda and D. Qi, Strategies for Reduced-Order Models for Predicting the Statistical Responses and Uncertainty Quantification in Complex Turbulent Dynamical Systems, *SIAM REVIEW* **60**, <https://doi.org/10.1137/16M1104664> (2018).

[10] B. Sanderse, Non-linearly stable reduced-order models for incompressible flow with energy-conserving finite volume methods, *Journal of Computational Physics* **421**, 109736 (2020).

[11] K. Hasselmann, Stochastic climate models part i. theory., *Tellus* **28**, 473 (1976).

[12] A. J. Majda, I. Timofeyev, and Vanden-Eijnden, Models for stochastic climate prediction, *Proc. Natl. Acad. Sci. USA* **96**, 14687–14691 (1999).

[13] A. Majda, C. Franzke, and D. Crommelin, Normal forms for reduced stochastic climate models, *Proc. Natl. Acad. Sci.* **10**, 3649–3653 (2010).

[14] M. Ghil and V. Lucarini, The physics of climate variability and climate change, *Rev. Mod. Phys.* **92**, 035002 (2020).

[15] V. Lucarini and M. Chekroun, Theoretical tools for understanding the climate crisis from Hasselmann’s programme and beyond, *Nat Rev Phys* (2023) (2023).

[16] V. Kitsios, L. Cordier, and T. J. O’Kane, Three-dimensional proper orthogonal decomposition reduced-order model of the global atmospheric climate, *International Journal of Heat and Fluid Flow* **119**, 110253 (2026).

[17] V. Kitsios, L. Cordier, and T. J. O’Kane, Proper orthogonal decomposition reduced-order model of the global oceans, *Theor. Comput. Fluid Dyn.* **38**, 707–727 (2024).

[18] C. Penland, Random Forcing and Forecasting Using Principal Oscillation Pattern Analysis, *Monthly Weather Review* **117**, 2165 (1989).

[19] I. Horenko, Finite element approach to clustering of multidimensional time series, *SIAM J. Sci. Comp.* **32**, 68–83 (2010).

[20] G. Pavliotis and A. Stuart, Parameter estimation for multiscale diffusions, *J. Stat. Phys.* **127**, 741–781 (2007).

[21] A. Majda and J. Harlim, Physics constrained nonlinear regression models for time series, *NONLINEARITY* **26**, 201–217 (2013).

[22] S. Kravtsov, D. Kondrashov, and M. Ghil, Multilevel Regression Modeling of Nonlinear Processes: Derivation and Applications to Climatic Variability , *Journal of Climate* **18**, 4404–4424 (2005).

[23] D. Kondrashov, M. Chekroun, and M. Ghil, Data-driven non-markovian closure models, *Physica D: Nonlinear Phenomena* **297**, 33 (2015).

[24] J. L. Callaham, J.-C. Loiseau, G. Rigas, and S. L. Brunton, Nonlinear stochastic modelling with langevin regression, *Proceedings of the Royal Society A: Mathematical, Physical and Engineering Sciences* **477**, 20210092 (2021), <https://royalsocietypublishing.org/rspa/article-pdf/doi/10.1098/rspa.2021.0092/725688/rspa.2021.0092.pdf>.

[25] A. Souza, Representing turbulent statistics with partitions of state space. part 1. theory and methodology., *J. Fluid Mech.* **997** (2024).

[26] N. Chen and A. J. Majda, Conditional gaussian systems for multiscale nonlinear stochastic systems: Prediction, state estimation and uncertainty quantification, *Entropy* **20**, 10.3390/e20070509 (2018).

[27] N. Chen and H. Liu, Minimum reduced-order models via causal inference, *Nonlinear Dyn* **113**, 11327–11351 (2025).

[28] L. Giorgini, Score-Based Modeling of Effective Langevin Dynamics, Arxiv <https://doi.org/10.48550/arXiv.2505.01895> (2025).

[29] R. Azencott, A. Beri, and I. Timofeyev, Adaptive subsampling for parametric estimation of gaussian diffusions, *J Stat Phys* **139**, 1066–1089 (2010).

[30] F. Ferretti, V. Chardès, T. Mora, A. M. Walczak, and I. Giardina, Building general langevin models from discrete datasets, *Phys. Rev. X* **10**, 031018 (2020).

[31] F. Falasca, Probing forced responses and causality in data-driven climate emulators: Conceptual limitations and the role of reduced-order models, *Phys. Rev. Res.* **7**, 043314 (2025).

[32] N. Geneva and N. Zabaras, Modeling the dynamics of pde systems with physics-constrained deep auto-regressive networks, *Journal of Computational Physics* **403**, 109056 (2020).

[33] M. Milano and P. Koumoutsakos, Neural network modeling for near wall turbulent flow, *Journal of Computational Physics* **182**, 1 (2002).

[34] P. Vlachas, G. Arampatzis, C. Uhler, and et al., Multiscale simulations of complex systems by learning their effective dynamics, *Nat Mach Intell* **4**, 359–366 (2022).

[35] J. Pathak, S. Subramanian, P. Harrington, S. Raja, A. Chattopadhyay, M. Mardani, T. Kurth, D. Hall, Z. Li, K. Azizzadenesheli, P. Hassanzadeh, K. Kashinath, and A. Anandkumar, FourCastNet: A Global Data-driven High-resolution Weather Model using Adaptive Fourier Neural Operators, arXiv e-prints , arXiv:2202.11214 (2022), arXiv:2202.11214 [physics.ao-ph].

[36] B. Bonev and et al., FourCastNet 3: A geometric approach to probabilistic machine-learning weather forecasting at scale, arXiv e-prints 10.48550/arXiv.2507.12144 (2025).

[37] O. Watt-Meyer, G. Dresdner, J. McGibbon, S. K. Clark, B. Henn, J. Duncan, N. D. Brenowitz, K. Kashinath, M. S. Pritchard, B. Bonev, M. E. Peters, and C. S. Bretherton, ACE: A fast, skillful learned global atmospheric model for climate prediction, arXiv e-prints , arXiv:2310.02074 (2023), arXiv:2310.02074 [physics.ao-ph].

[38] O. Watt-Meyer, B. Henn, J. McGibbon, S. K. Clark, A. Kwa, W. A. Perkins, and C. S. Bretherton, ACE2: Accurately learning subseasonal to decadal atmospheric variability and forced responses, arXiv e-prints <https://arxiv.org/abs/2411.11268> (2024).

[39] H. Guan, T. Arcaman, A. Chattopadhyay, and R. Maulik, LUCIE: A Lightweight Uncoupled Climate Emulator with long-term stability and physical consistency for O(1000)-member ensembles, arXiv <https://doi.org/10.48550/arXiv.2405.16297> (2025).

[40] W. Chapman, J. Schreck, Y. Sha, D. Gagne II, D. Kimpara, L. Zanna, K. Mayer, and J. Berner, CAMulator: Fast Emulation of the Community Atmosphere Model, Arxiv <https://doi.org/10.48550/arXiv.2504.06007> (2025).

[41] S. Dheeshjith, A. Subel, A. Adcroft, J. Busecke, C. Fernandez-Granda, S. Gupta, and L. Zanna, Samudra: An AI global ocean emulator for climate., *Geophysical Research Letters* **52**, e2024GL114318 (2025).

[42] T. Beucler, M. Pritchard, S. Rasp, J. Ott, P. Baldi, and P. Gentine, Enforcing analytic constraints in neural networks emulating physical systems, *Phys. Rev. Lett.* **126**, 098302 (2021).

[43] N. Mücke and B. Sanderse, Physics-aware generative models for turbulent fluid flows through energy-consistent stochastic interpolants, Arxiv <https://doi.org/10.48550/arXiv.2504.05852> (2025).

[44] X. Tian, D. Holdaway, and D. Kleist, Evaluating machine learning weather models for data assimilation: Fundamental limitations in tangent linear and adjoint properties, *Geophysical Research Letters* **53**, e2025GL119402 (2026).

[45] S. Van Loon, M. Rugenstein, and E. A. Barnes, Reanalysis-based Global Radiative Response to Sea Surface Temperature Patterns: Evaluating the Ai2 Climate Emulator, *Geophysical Research Letters* **52**, e2025GL115432 (2025).

[46] B. Zhang and T. Merlis, The Equilibrium Response of Atmospheric Machine-Learning Models to Uniform Sea Surface Temperature Warming, Arxiv <https://doi.org/10.48550/arXiv.2510.02415> (2026).

[47] J. Ismael, Reflections on the asymmetry of causation, *Interface Focus* **12**, 20220081 (2023).

[48] E. Aurell and G. Del Ferraro, Causal analysis, correlation- response, and dynamic cavity, *J. of Phys.: Conference Series* **699**, 012002 (2016).

[49] V. Lucarini, Revising and Extending the Linear Response Theory for Statistical Mechanical Systems: Evaluating Observables as Predictors and Predictands, *J Stat Phys* **173**, 1698–1721 (2018).

[50] D. Lucente, M. Baldovin, F. Cecconi, M. Cencini, N. Coccaglia, A. Puglisi, M. Viale, and A. Vulpiani, Conceptual and practical approaches for investigating irreversible processes, *New Journal of Physics* **27**, 041201 (2025).

[51] T. Paus, Inferring causality in brain images: a perturbation approach, *Philos Trans R Soc Lond B Biol Sci.* **29**, 041201 (2005).

[52] J. Bloch-Johnson, M. A. A. Rugenstein, M. J. Alessi, C. Prostosescu, M. Zhao, B. Zhang, A. I. L. Williams, J. M. Gregory, J. Cole, Y. Dong, M. L. Duffy, S. M. Kang, and C. Zhou, The green's function model intercomparison project (gfmip) protocol, *Journal of Advances in Modeling Earth Systems* **16**, e2023MS003700 (2024).

[53] R. H. Kraichnan, Classical fluctuation-relaxation theorem, *Phys. Rev.* **113**, 1181 (1959).

[54] M. Falcioni, S. Isola, and A. Vulpiani, Correlation functions and relaxation properties in chaotic dynamics and statistical mechanics, *Physics Letters A* **144**, 341 (1990).

[55] A. J. Majda, R. V. Abramov, and M. J. Grote, *Information Theory and Stochastics for Multiscale Nonlinear Systems* (CRM Monograph Series, American Mathematical Society, 2005).

[56] U. Marconi, A. Puglisi, L. Rondoni, and A. Vulpiani, Fluctuation-dissipation: Response theory in statistical physics, *Phys. Rep.* **461** (2008).

[57] A. Gritsun and G. Branstator, Climate response using a three-dimensional operator based on the fluctuation-dissipation theorem, *Journal of The Atmospheric Science* , 2558–2575 (2007).

[58] V. Lucarini, M. S. Gutiérrez, J. Moroney, and N. Zagli, A general framework for linking free and forced fluctuations via koopmanism, *Chaos, Solitons & Fractals* **202**, 117540 (2026).

[59] M. Baldovin, F. Cecconi, and A. Vulpiani, Understanding causation via correlations and linear response theory, *Physical Review Research* **2**, 043436 (2020).

[60] F. Cecconi, G. Costantini, C. Guardiani, M. Baldovin, and A. Vulpiani, Correlation, response and entropy approaches to allosteric behaviors: a critical comparison on the ubiquitin case, *Physical Biology* **20**, 056002 (2023).

[61] M. Baldovin, F. Cecconi, A. Provenzale, and A. Vulpiani, Extracting causation from millennial-scale climate fluctuations in the last 800 kyr, *Scientific Reports* **12**, 15320 (2022).

[62] F. Falasca, P. Perezhogin, and L. Zanna, Data-driven dimensionality reduction and causal inference for spatiotemporal climate fields, *Phys. Rev. E* **109**, 044202 (2024).

[63] F. Falasca, A. Basinski, L. Zanna, and M. Zhao, A fluctuation-dissipation theorem perspective on radiative responses to temperature perturbations, Arxiv <https://doi.org/10.48550/arXiv.2408.12585> (2025).

[64] T. Alberti, M. Stumpo, F. Florindo, and E. J. Rohling, Cause-and-effect relationships between sea surface temperature changes in different regions during the past 4.5 million years, *Paleoceanography and Paleoclimatology* **40**, e2024PA004936 (2025).

[65] L. Giorgini, F. Falasca, and A. Souza, Predicting Forced Responses of Probability Distributions via the Fluctuation-Dissipation Theorem and Generative Modeling, Arxiv <https://doi.org/10.48550/arXiv.2504.13333> (2025).

[66] J. Charney and J. DeVore, Multiple flow equilibria in the atmosphere and blocking, *Journal of the atmospheric sciences* **36**, 1205 (1979).

[67] A. Majda, B. Gershgorin, and Y. Yuan, Low-Frequency Climate Response and Fluctuation–Dissipation Theorems: Theory and Practice , *Journal of the Atmospheric Sciences* **67**, 1186–1201 (2010).

[68] A. Majda, R. Abramov, and B. Gershgorin, High skill in low-frequency climate response through fluctuation dissipation theorems despite structural instability, *Proc. Natl. Acad. Sci.* **107**, 581–586 (2010).

[69] L. T. Giorgini, K. Deck, T. Bischoff, and A. Souza, Response theory via generative score modeling, *Phys. Rev. Lett.* **133**, 267302 (2024).

[70] D. Ruelle, General linear response formula in statistical mechanics, and the fluctuation-dissipation theorem far from equilibrium, *Physics Letters A* **245**, 220 (1998).

[71] D. Ruelle, A review of linear response theory for general differentiable dynamical systems, *Nonlinearity* **22**, 855 (2009).

[72] M. Colangeli, L. Rondoni, and A. Vulpiani, Fluctuation-dissipation relation for chaotic non-hamiltonian systems, *Journal of Statistical Mechanics: Theory and Experiment* **2012**, L04002 (2012).

[73] C. E. Leith, Climate response and fluctuation dissipation, *Journal of The Atmospheric Science* **32**, 2022–2026 (1975).

[74] Y. Song, J. Sohl-Dickstein, D. P. Kingma, A. Kumar, S. Ermon, and B. Poole, Score-based generative modeling through stochastic differential equations, arXiv preprint arXiv:2011.13456 <https://doi.org/10.48550/arXiv.2011.13456> (2021).

[75] Y. Song, S. Garg, J. Shi, and S. Ermon, Sliced score matching: A scalable approach to density and score estimation, arXiv preprint arXiv.1905.07088 <https://doi.org/10.48550/arXiv.1905.07088> (2021).

[76] C. Pedersen, L. Zanna, and J. Bruna, Thermalizer: Stable autoregressive neural emulation of spatiotemporal chaos, Arxiv <https://doi.org/10.48550/arXiv.2503.18731> (2025).

[77] A. Souza, S. Silvestri, K. Deck, T. Bischoff, R. Ferrari, and G. Flierl, Surface to seafloor: A generative ai framework for decoding the ocean interior state, arXiv preprint <https://doi.org/10.48550/arXiv.2504.15308> (2025).

[78] I. Price, A. Sanchez-Gonzalez, F. Alet, and et al., Probabilistic weather forecasting with machine learning, *Nature* **637**, 84–90 (2025).

[79] N. Brenowitz and et al., Climate in a bottle: Towards a generative foundation model for the kilometer-scale global atmosphere, arXiv preprint arXiv.2505.06474 <https://doi.org/10.48550/arXiv.2505.06474> (2025).

[80] A. Lobbe, D. Crisan, and O. Lang, Bayesian inference for geophysical fluid dynamics using generative models, *Philosophical Transactions of the Royal Society A: Mathematical, Physical and Engineering Sciences* **383**, 20240321 (2025), <https://royalsocietypublishing.org/rsta/article-pdf/10.1098/rsta.2024.0321/2819094/rsta.2024.0321.pdf>.

[81] A. Hyvärinen, Estimation of non-normalized statistical models by score matching, *Journal of Machine Learning Research* **6**, 695–709 (2005).

[82] F. Pedregosa, G. Varoquaux, A. Gramfort, V. Michel, B. Thirion, O. Grisel, M. Blondel, P. Prettenhofer, R. Weiss, V. Dubourg, J. Vanderplas, A. Passos, D. Cournapeau, M. Brucher, M. Perrot, and E. Duchesnay, Scikit-learn: Machine learning in Python, *Journal of Machine Learning Research* **12**, 2825 (2011).

[83] A. Paszke and et al., PyTorch: An Imperative Style, High-Performance Deep Learning Library, Arxiv

<https://doi.org/10.48550/arXiv.1912.01703> (2025).

[84] Y. Chen, M. Goldstein, M. Hua, M. Albergo, N. Boffi, and E. Vanden-Eijnden, Probabilistic Forecasting with Stochastic Interpolants and Föllmer Processes, Arxiv <https://doi.org/10.48550/arXiv.2403.13724> (2025).

[85] E. Lorenz, Deterministic nonperiodic flow, *J. Atmospheric Sci.* **20**, 130–141 (1963).

[86] P. Cvitanović, R. Artuso, R. Mainieri, G. Tanner, and G. Vattay, *Chaos: Classical and Quantum* (ChaosBook.org, Niels Bohr Institute, Copenhagen, 2016).

[87] R. Miranda and E. Stone, The proto-lorenz system, *Physics Letters A* **178**, 105 (1993).

[88] C. Penland and P. Sardeshmukh, The optimal growth of tropical sea surface temperature anomalies, *Journal of Climate* **8**, 1999–2024 (1995).

[89] C. Penland, A stochastic model of indopacific sea surface temperature anomalies, *Physica D: Nonlinear Phenomena* **98**, 534 (1996), *nonlinear Phenomena in Ocean Dynamics*.

[90] C. Penland, M. D. Fowler, D. L. Jackson, and R. Cifelli, Forecasts of opportunity for northern california soil moisture, *Land* **10**, 10.3390/land10070713 (2021).

[91] Y. Zhao and A. Capotondi, The role of the tropical Atlantic in tropical Pacific climate variability, *npj Clim Atmos Sci* **7** (2024).

[92] E. Guderian, W. Han, P. Webster, L. Zhang, and M. Di Lorenzo, Investigating the relative contribution from tropical indo-pacific sst to asian monsoon precipitation variability using lim, *Journal of Climate* , 6201–6219 (2024).

[93] A. J. Majda and B. Gershgorin, Improving model fidelity and sensitivity for complex systems through empirical information theory, *Proceedings of the National Academy of Sciences* **108**, 10044 (2011), <https://www.pnas.org/doi/pdf/10.1073/pnas.1108132108>.

[94] A. J. Majda and B. Gershgorin, Link between statistical equilibrium fidelity and forecasting skill for complex systems with model error, *Proceedings of the National Academy of Sciences* **108**, 12599 (2011), <https://www.pnas.org/doi/pdf/10.1073/pnas.1108132108>.

[95] H. De Swart, Low-order spectral models of the atmospheric circulation: A survey, *Acta Applicandae Mathematica* **11**, 49 (1988).

[96] D. Crommelin and A. Majda, Strategies for Model Reduction: Comparing Different Optimal Bases, *Journal of the Atmospheric Sciences* **61**, 2206–2217 (2004).

[97] D. T. Crommelin, J. Opsteegh, and F. Verhulst, A mechanism for atmospheric regime behavior, *Journal of the atmospheric sciences* **61**, 1406 (2004).

[98] J. Dorrington and T. Palmer, On the interaction of stochastic forcing and regime dynamics, *Nonlinear Processes in Geophysics* **30**, 49 (2023).

[99] T. Grafke and E. Vanden-Eijnden, Numerical computation of rare events via large deviation theory, *Chaos: An Interdisciplinary Journal of Nonlinear Science* **29** (2019).

[100] A. J. Majda, I. Timofeyev, and Vanden-Eijnden, A mathematical framework for stochastic climate models, *Proc. Natl. Acad. Sci. USA* **54**, 891–974 (2001).

[101] C. Franzke and A. Majda, Low-order stochastic mode reduction for a prototype atmospheric GCM, *Journal of the Atmospheric Sciences* **2**, 457–479 (2006).

[102] J. Berner and G. Branstator, Linear and nonlinear signatures in the planetary wave dynamics of an agcm: Probability density functions, *Journal of the Atmospheric Sciences* **64**, 117–136 (2007).

[103] P. Sura, M. Newman, C. Penland, and P. Sardeshmukh, Multiplicative noise and non-Gaussianity: A paradigm for atmospheric regimes?, *Journal of Climate* **62**, 1391–1409 (2005).

[104] L. Onsager and S. Machlup, Fluctuations and irreversible processes, *Phys. Rev.* **91**, 1505 (1953).

[105] G. Di Antonio and G. V. Vinci, Nonlinear correlations underlie linear response and causality, *Phys. Rev. Res.* **7**, L042029 (2025).

[106] J. Nathaniel, C. Roesch, J. Buch, and et al., Deep Koopman operators for causal discovery, *Commun Phys* **8**, <https://doi.org/10.1038/s42005-025-02426-1> (2025).

[107] A. Zhou, A. Wikner, A. Lancelin, P. Hassanzadeh, and A. B. Farimani, Reframing Generative Models for Physical Systems using Stochastic Interpolants, Arxiv <https://doi.org/10.48550/arXiv.2509.26282> (2025).

[108] M. Hutchinson, A stochastic estimator of the trace of the influence matrix for laplacian smoothing splines, *Communications in Statistics-Simulation and Computation* **18**, 1059–1076 (1989).

[109] E. Lorenz, Predictability: a problem partly solved, *Seminar on Predictability*, 4–8 September 1995 **1**, 1 (1995).

[110] S. Kravtsov, M. Ghil, and D. Kondrashov, Empirical Model Reduction and the Modeling Hierarchy in Climate Dynamics and the Geosciences, in *Stochastic Physics and Climate Modeling*, edited by T. Palmer and P. Williams (Cambridge University Press, 2009) pp. 35–72.

[111] K. Strounine, S. Kravtsov, D. Kondrashov, and M. Ghil, Reduced models of atmospheric low-frequency variability: Parameter estimation and comparative performance, *Physica D: Nonlinear Phenomena* **239**, 145 (2010).

[112] D. P. Kingma and J. Ba, Adam: A method for stochastic optimization, arXiv preprint arXiv:1412.6980 (2014).

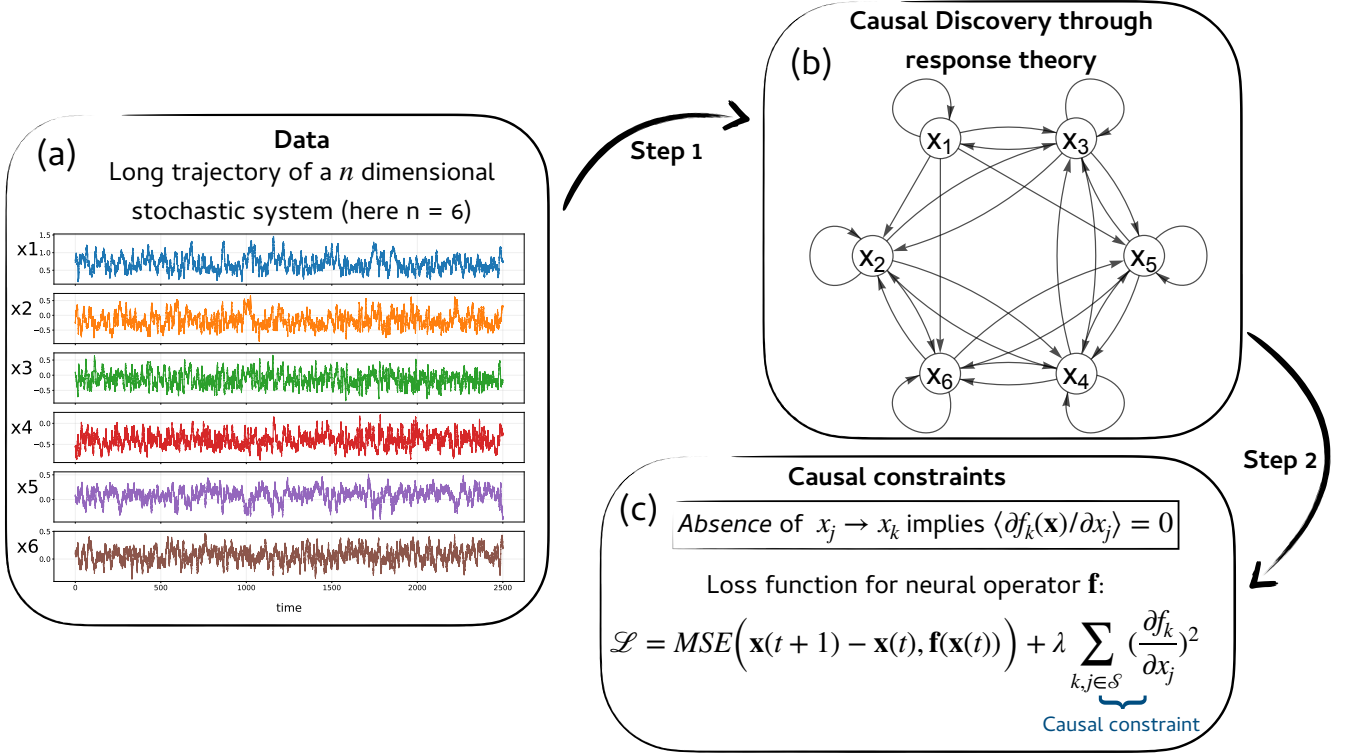


FIG. 1: Schematic of the proposed framework. Step 1: From a long trajectory of a Markovian system, the Fluctuation–Dissipation Theorem is used to infer the system’s causal structure. Step 2: This inferred structure is then imposed as a soft constraint during neural-network training, yielding causally constrained emulators. The example shows time series from the Charney–DeVore model (Eq. (3) in the main text) and the discovered causal graph, but the approach applies to general stochastic dynamical systems.

Supplemental Material for: Causally constrained reduced-order neural climate emulators via response theory

Fabrizio Falasca and Laure Zanna

Courant Institute School of Mathematics, Computing and Data Science, New York University

(Dated: February 17, 2026)

I. FLUCTUATION-DISSIPATION THEOREM (FDT) FROM DATA: QUASI-GAUSSIAN AND SCORE MATCHING

The FDT. Consider a n -dimensional system $\mathbf{x}(t) = [x_1, x_2, \dots, x_n](t)$. The Fluctuation-Dissipation Theorem (FDT) states that the time-dependent response of an observable $A(x_k(t))$ to a small impulse perturbation $\delta x_j(0)$ imposed on $x_j(0)$ at time $t = 0$, can be retrieved solely from stationary statistics of the system as:

$$R_{k,j}(t) = \lim_{\delta x_j(0) \rightarrow 0} \frac{\delta \langle A(x_k(t)) \rangle}{\delta x_j(0)} = - \left\langle x_k(t) \frac{\partial \ln \rho(\mathbf{x})}{\partial x_j} \Big|_{\mathbf{x}(0)} \right\rangle. \quad (1)$$

where $\rho(\mathbf{x})$ represents the invariant probability distribution of the system [54, 56]. The FDT establishes a link between perturbed quantities and stationary statistics, i.e. the invariant measure of the system [55, 56]. The brackets $\langle \cdot \rangle$ represents ensemble averages, in practice computed using temporal averages under the assumption of ergodicity. Application of the FDT in the main text focused on the observable $A(x_k(t)) = x_k(t)$. In this case, Eq. 1 represents the impulse response in the ensemble mean.

A. The FDT from data

Quasi-Gaussian (qG) approximation. A long standing problem in inferring the FDT response operator is the need to estimate the gradients of logarithm of the invariant distribution $s(\mathbf{x}) = \nabla \ln \rho(\mathbf{x})$, the so-called *score function* [81]. Traditionally, the quasi-Gaussian (qG) approximation has been used [55, 73], by replacing $\rho(\mathbf{x})$ by a Gaussian distribution $\rho^G(\mathbf{x})$ with the same mean and second moments. In this case the score can be directly is:

$$s^G(\mathbf{x}) = \nabla \ln \rho^G(\mathbf{x}) = -\boldsymbol{\Sigma}^{-1}(\mathbf{x} - \boldsymbol{\mu}). \quad (2)$$

$\boldsymbol{\mu} \in \mathbb{R}^n$ and $\boldsymbol{\Sigma} \in \mathbb{R}^{n,n}$ are the mean and covariance matrix of the data, respectively. Note, that while a Gaussian approximation is used for $\rho(\mathbf{x})$, the response formula in Eq. (1) is still computed over the original invariant measure [55, 65]. In other words, this approximation differs from linear inverse model strategies which assume a Gaussian measure from the outset. The qG approximation has high skill in predicting responses in the ensemble mean even in nonlinear systems [55, 57, 59] but it can introduce biases for higher order moments [65, 67].

Score-based generative modeling and FDT. Recent advances in generative modeling provide novel tools for estimating the score function directly from data, overcoming assumptions such as the qG approximation. In particular, [74] showed that score estimation can be recasted as a denoising problem. This led to scalable diffusion models that integrate a reverse-time Langevin equation from a reference distribution (typically Gaussian) toward the data distribution [76]. As in the FDT framework, a central object of these frameworks is the score function. Giorgini et al. (2024) [69], first proposed to use denoising score matching strategies in the FDT context. In practice, the true score on the system's attractor can be then approximated by the score of a distribution perturbed with a small amount of noise [69]. This strategy has been successfully applied to stochastic dynamical systems of increasing complexity [65, 69]. The broader appeal of this approach is its connection between established ideas from statistical physics (FDT) and modern generative modeling.

Score matching. In this study, we extended the prior work in [65, 69] by learning the score directly on the attractor using the classic result of Hyvärinen (2005) [81], hereafter “score matching”. Given T samples of a n dimensional dynamical system $\mathbf{x} \in \mathbb{R}^{T,n}$, we parameterize the score function $s_\theta(\mathbf{x})$ with a neural network s and parameters θ . Specifically, s_θ is approximated with a multilayer perceptron (MLP). The network is trained by minimizing the following loss:

$$\mathbb{E}_{\rho(x)}[\text{tr}(\nabla_{\mathbf{x}} s_\theta(\mathbf{x})) + \frac{1}{2} \|s_\theta(\mathbf{x})\|_2^2], \quad (3)$$

where the expectation $\mathbb{E}_{\rho(x)}$ is approximated by a time average over the available samples. The specific implementation used in this work relies on an approximation similar to the sliced score-matching approach proposed in [75]. Specifically, we considered the Hutchinson Trace Estimation [108] to compute the trace in Eq. (3). As in Giorgini et al. (2025) [65], in the case of high-dimensional dynamics we suggest using the common denoising score matching implemented with a U-Net architecture.

Practical considerations and correction procedure. The score-matching procedure introduced by Hyvärinen (2005) [81] provides an elegant way to estimate the score $s(\mathbf{x})$ directly on the system's inertial manifold. In practice, however, this estimation can be prone to several sources of error. First, ensemble averages must be replaced by empirical averages computed from finite datasets. Second, the inferred score inevitably depends on the chosen neural-network architecture and its associated hyperparameters. Nevertheless, the theoretical formalism of the FDT, provides analytical constraints on the instantaneous response $\mathbf{R}(t = 0)$. As shown in [69], these constraints can be used as a posteriori correction of the estimated score, thereby ensuring reliable results. Such corrections are non-unique, but they typically produce only small adjustments to the inferred response and thus eliminate the need for more sophisticated architectures. In what follows, we detail the analytical correction for score-based estimates relevant to the ensemble-mean response. We denote the ideal score by $s(\mathbf{x})$, the score inferred through score matching by $s_\epsilon(\mathbf{x})$, and the corrected score by $s_c(\mathbf{x})$. The system's dynamics is encoded in a data matrix $\mathbf{x} \in \mathbb{R}^{T,n}$, where T is the number of temporal samples and n the system's dimensionality. The correction procedure is dependent on the type of response analyzed. If the interest is in the response in ensemble mean, i.e. observable $A(x_k(t)) = x_k(t)$ in Eq. (1), then it is possible to use the correction already outlined in [69]. The response operator in the ensemble mean at time $t = 0$ of any system is:

$$\mathbf{R}(0) = \mathbf{I} \quad (4)$$

\mathbf{I} being the identity matrix. The empirical estimation of the instantaneous response operator with the inferred score $s_\epsilon(\mathbf{x})$ will lead to small errors, so that

$$\mathbf{R}_\epsilon(0) = -\frac{1}{T} \mathbf{x}^T \cdot s_\epsilon(\mathbf{x}) = \mathbf{I} - \epsilon \quad (5)$$

where $\mathbf{R}_\epsilon(0)$ denotes the estimated response. It is then possible to correct the inferred score as:

$$s_c(\mathbf{x}) = s_\epsilon(\mathbf{x}) \cdot (\mathbf{I} - \epsilon)^{-1}. \quad (6)$$

The corrected score $s_c(\mathbf{x})$ defined in Eq. (6) guarantees the equivalence Eq. (4) and it is the one used in the computation of responses in ensemble mean in the main text. Note that while this correction is non-unique, different versions lead to small differences as argued in the SM of [28].

Response operator via score matching: response in the ensemble mean. Given the proposed correction in Eq. (6), we now infer the response operator for the Charney-DeVore system in Eq. (3) in the main text. We compare the prediction of the qG approximation and the score-matching estimation against the the numerical ground truth and show the results in Figure 2. First, we note that the quasi-Gaussian approximation leads to good, first-order results even in a strongly nonlinear model such as the Charney-DeVore model. The FDT inferred through score matching is generally more accurate than the quasi-Gaussian approximation.

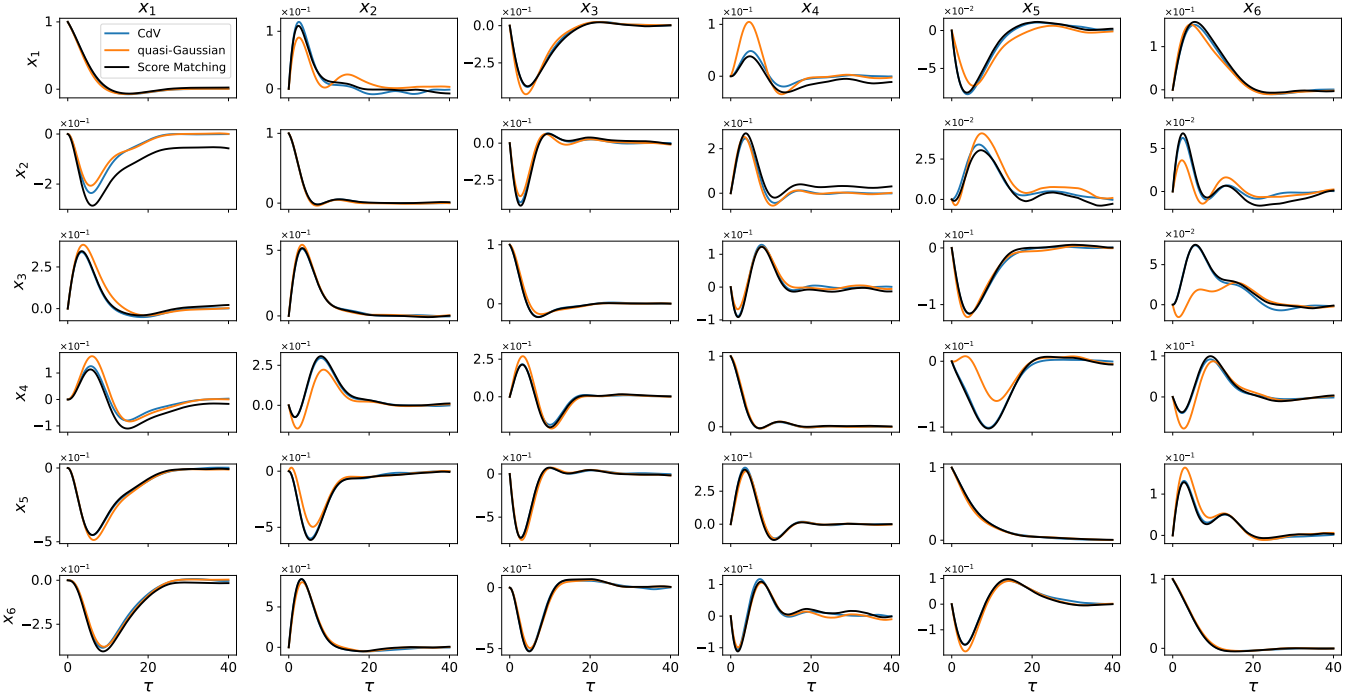


FIG. 2: Time-dependent, responses in ensemble mean $x_k(t)$ to an impulse perturbation in the CdV model (Eq. (3) in the main text) as predicted by the FDT using the quasi-Gaussian and score-matching approximations. Example: column (1), row (2) quantifies the time-dependent mean response of $x_{k-2}(t)$ given a small, impulse perturbation imposed on $x_{j=1}(0)$ at time $t = 0$.

II. POSSIBLE LIMITATIONS OF THE CAUSAL CONSTRAINTS AND PRACTICAL CONSIDERATIONS

Causal relations in high-dimensional stochastic dynamical systems are most naturally, and practically, identified at the level of ensemble-averaged quantities [31]. Specifically, the response operator at the shortest time-scale can be written in terms of the ensemble averaged Jacobian as $\mathbf{R}(dt) = \langle \mathbf{J}(\mathbf{x}) \rangle dt + \mathbf{I}$, where $\mathbf{J}(\mathbf{x})$ denotes the Jacobian, \mathbf{I} is the identity matrix, and $dt \rightarrow 0$. Accordingly, the causal constraints introduced in the main text, exploit vanishing entries of the ensemble-averaged Jacobian, $\langle \partial f_k(\mathbf{x}) / \partial x_j \rangle = 0$, to suppress the corresponding state-dependent couplings $\partial f_k(\mathbf{x}) / \partial x_j$ in the neural network loss. In other words, the central assumption of this work is that knowledge of the zeros of the ensemble averaged Jacobian already provides an informative constraint for guiding the architecture of general neural emulators. A complication arises in idealized systems with exact symmetries, such as the Lorenz '63 and Lorenz '96 systems [85, 109]. In such cases $R_{k,j}(dt) = 0$ can arise from exact cancellations in the ensemble average, even though $\partial f_k(\mathbf{x}) / \partial x_j \neq 0$ pointwise. In such cases, a vanishing short-time response does not necessarily imply the absence of an instantaneous coupling. One possible strategy in such idealized settings is to explicitly reduce the symmetries of the underlying dynamical system, following symmetry-reduction approaches as advocated in [86]. For example, in the Lorenz '63 system [85], this corresponds to considering the so-called "proto-Lorenz" system [87], in which the symmetries of the original system are reduced. More importantly, however, we argue that this limitation does not constitute a practical obstacle for reduced-order modeling of real-world turbulent climate systems, which are the primary focus of this work. Such systems typically lack exact symmetries and admit no unique coarse-grained representation. The effective drift term \mathbf{f} is validated on its ability to reproduce stationary and statistics given a specific choice of coarse-grained representation. In this context, we find it useful to provide additional qualitative justification for why focusing on zeros of the ensemble-averaged Jacobian is not a fundamental limitation. First, we discuss a qualitative mathematical argument in the context of linear inverse models of climate. Second, we emphasize a more general point regarding the non-uniqueness of effective dynamics in data-driven modeling of coarse-grained systems.

- In the context of reduced-order modeling of large-scale climate variability, typically constructed from anomalies, there is extensive evidence that linear inverse models (LIMs), i.e. $d\mathbf{x} = \mathbf{L}\mathbf{x}dt + \Sigma d\mathbf{W}$, as originally proposed by Penland [18], provide a useful effective approximation of the dynamics and serve as powerful forecasting tools; see [18, 88–92] among many others. A natural generalization incorporates quadratic nonlinearities,

$$d\mathbf{x} = (\mathbf{L}\mathbf{x} + \mathbf{B}(\mathbf{x}, \mathbf{x}))dt + \Sigma d\mathbf{W}$$

as discussed, for example, in [55]. In what follows, we focus on nonlinear extensions of the LIM within this quadratic framework. In this case, the k -th component of the drift can be written as

$$f_k(\mathbf{x}) = \sum_m L_{k,m} x_m + \sum_{m,n} B_{k,m,n} x_m x_n .$$

and the corresponding Jacobian entry takes the form

$$J_{k,j}(\mathbf{x}) = \partial f_k(\mathbf{x}) / \partial x_j = L_{k,j} + \sum_m B_{k,j,m} x_m + \sum_n B_{k,n,j} x_n .$$

Taking the ensemble average yields

$$\langle J_{k,j}(\mathbf{x}) \rangle = \langle \partial f_k(\mathbf{x}) / \partial x_j \rangle = L_{k,j} + \sum_m B_{k,j,m} \langle x_m \rangle + \sum_n B_{k,n,j} \langle x_n \rangle .$$

In the common modeling regime where climate variability is represented in terms of anomalies, one typically has $\langle x_n \rangle = 0$ for all components, leading to

$$\langle J_{k,j}(\mathbf{x}) \rangle = L_{k,j} .$$

In this modeling setting, the ensemble-averaged Jacobian therefore coincides with the linear operator \mathbf{L} . The empirical success of linear inverse models for coarse-grained climate variability suggests that, at this level of coarse-grained description (typically around 20 principal components of a given climate field, see e.g. [88]), the linear operator \mathbf{L} approximates the dominant direct couplings, with nonlinear terms acting as corrections. This linear operator is obviously state independent. As a result, in this example, any vanishing entry $\langle J_{k,j} \rangle = L_{k,j} = 0$ reflects the absence of a linear coupling, rather than a cancellation induced by ensemble averaging, therefore providing intuition for why vanishing entries of the ensemble-averaged Jacobian are structurally meaningful constraints.

- More broadly, this work highlights a principle relevant to data-driven modeling of realistic multiscale systems. As discussed in [31], the effective drift \mathbf{f} inferred from data is inherently non-unique and depends on modeling choices such as variable selection, resolution, filtering, and projection onto latent representations. In this setting, there is no single “true” dynamics; instead, models are evaluated by their ability to reproduce stationary and perturbed statistics at the chosen level of coarse graining. From this perspective, a vanishing short-time response $R_{k,j}(dt) = 0$ provides sufficient justification to construct an effective model

$$d\mathbf{x} = \mathbf{f}(\mathbf{x})dt + \Sigma(\mathbf{x})d\mathbf{W}$$

in which the structural constraint $\partial f_k(\mathbf{x})/\partial x_j = 0$ is explicitly enforced. The validity of such constraints is then assessed by the accuracy of the resulting stationary and forced responses, rather than by comparison to a non-existent unique underlying dynamics.

Assessment of causal constraints. Finally, causally constrained emulators can be readily compared with an unconstrained counterpart by evaluating their representation of the linear response operator against the FDT-based estimate in Eq. (1) of the main text. Such comparisons should be performed at short time lags in order to avoid spurious responses that may arise at longer lags when using the FDT [62]. The causal constraints introduced here should be applied when they improve the representation of the response operator relative to the unconstrained model. In systems with exact symmetries, as discussed above, any biases introduced by the constraints will already be apparent in the representation of stationary variability.

III. DETAILS ON THE EMULATOR FORMULATIONS

We report the main technical details for fitting the emulators in the main text. This Section follows Appendix C in [31] and we refer to that work for more details. Consider a n -dimensional dynamical system described by a stochastic differential equation $d\mathbf{x} = \mathbf{f}(\mathbf{x})dt + \Sigma d\mathbf{W}$. This equation can be discretized by the forward Euler method as follows:

$$\Delta\mathbf{x} = \mathbf{x}(t + \Delta t) - \mathbf{x}(t) = \mathbf{f}(\mathbf{x}(t))\Delta t + \Sigma\sqrt{\Delta t}\xi(t) \quad (7)$$

where $\xi(t)$ is a Gaussian white noise with zero mean, unit variance, and $\sqrt{\Delta t}\xi(t)$ is the increment of the Wiener process $\Delta\mathbf{W} = \mathbf{W}(t + \Delta t) - \mathbf{W}(t)$. Without loss of generality, we rescale time units by the time sampling interval such that a non-dimensional time increment is $\Delta t = 1$ [22, 23, 110, 111]. The strategy is then to fit a rescaled version of Eq. (7) from observational data alone. Such rescaled equation takes the following form:

$$\Delta\mathbf{x} = \mathbf{x}(t + 1) - \mathbf{x}(t) = \mathbf{f}(\mathbf{x}(t)) + \Sigma\xi(t). \quad (8)$$

In what follows, we will not distinguish between the original model terms (e.g., \mathbf{f}) and their emulator counterparts, in order to avoid unnecessary notation and maintain a clear and concise presentation. We explicitly clarify the distinction whenever it becomes relevant. We proceed in two steps: fitting the deterministic drift and then the stochastic noise. We first focus on fitting the drift. We compute $\Delta\mathbf{x} = \mathbf{x}(t + 1) - \mathbf{x}(t)$ and fit the deterministic dynamics such that $\Delta\mathbf{x} \approx \mathbf{f}(\mathbf{x}(t))$. In the main paper, we considered two cases:

- Unconstrained drift.* The vanilla emulator is trained to minimize the MSE between $\Delta\mathbf{x}$ and $\mathbf{f}(\mathbf{x}(t))$ as:

$$\mathcal{L} = MSE(\Delta\mathbf{x}, \mathbf{f}(\mathbf{x})). \quad (9)$$

The model \mathbf{f} is fitted by a multilayer perceptron (MLP). The MSE is minimized using a version of the gradient descent algorithm (Adam, [112]) with weight decay. The MLP considered here always consisted of one hidden layer with 100 neurons. We found empirically that adding more layers can lead to instabilities even in stationary runs, while opting for a shallow, but wide network led to stable simulations. The activation function used is the swish function (SiLU), which we found yields smoother responses to external perturbations.

- Causally constrained drift.* Here we consider the same architecture of the unconstrained drift above. The main difference is in the loss function, here equal to:

$$\mathcal{L} = MSE(\Delta\mathbf{x}, \mathbf{f}(\mathbf{x})) + \lambda \sum_{k,j \in \mathcal{S}} \left(\frac{\partial f_k}{\partial x_j} \right)^2, \quad (10)$$

where the set of entries (k, j) is determined by the causal Adjacency matrix introduced in the main text. The derivative $\partial f_k / \partial x_j$ are computed with Autograd from PyTorch, providing automatic differentiation [83]. λ is here set to $\lambda = 10$.

Once a deterministic drift \mathbf{f} is computed we close the equation with a Wiener process. The first step is to compute the residuals of the deterministic dynamics as $\mathbf{r}(t) = \Delta\mathbf{x} - \mathbf{f}(\mathbf{x}(t))$, $\mathbf{r}(t) \in \mathbb{R}^n$. A stochastic parametrization for this residual term is then constructed. As the main paper is focused on proposing constraints acting on the drift term, we adopted the simplest option, in which the noise term in Eq. (8) is diagonal, with each entry (i, i) given by the standard deviation of $r_i(t)$. For details on more complex stochastic closure, such as state-dependent noise we refer to the work of Falasca (2025) [31].

IV. CHARNEY DE-VORE MODEL: PARAMETERS

The values of the parameters used for the Charney-DeVore model (Eq. (3) in the main text) are reported in Table I below. All parameters are chosen with standard values as discussed in [65, 95, 97, 98]. The system is integrated using a Euler-Maruyama scheme with $dt = 0.01$.

TABLE I: Model coefficients for the six-dimensional stochastic Charney-DeVore model.

| Parameter | Value | Description |
|----------------------|----------------------------------------------------------------------|-----------------------------------|
| C | 0.1 | Newtonian relaxation rate |
| x_1^* | 0.95 | Zonal background forcing (mode 1) |
| x_4^* | -0.76095 | Zonal background forcing (mode 4) |
| γ | 0.2 | Topographic height |
| b | 1.6 | Channel aspect ratio |
| α_m | $\frac{8\sqrt{2}}{\pi} \frac{m^2}{4m^2-1} \frac{b^2+m^2-1}{b^2+m^2}$ | Nonlinear advection (mode m) |
| β_m | $\frac{\beta b^2}{b^2+m^2}$ | Coriolis effects (mode m) |
| δ_m | $\frac{64\sqrt{2}}{15\pi} \frac{b^2+m^2+1}{b^2+m^2}$ | Triad interaction (mode m) |
| γ_m | $\gamma \frac{4m^3}{4m^2-1} \frac{\sqrt{2}b}{\pi(b^2+m^2)}$ | Orographic damping (mode m) |
| $\tilde{\gamma}_m^*$ | $\gamma \frac{4m}{4m^2-1} \frac{\sqrt{2}b}{\pi}$ | Orographic forcing (mode m) |
| ε | $\frac{16\sqrt{2}}{5\pi}$ | Wave-wave interaction |
| σ | 0.05 | Noise amplitude |
| dt | 0.01 | Integration time step |

V. PRACTICAL ESTIMATION OF THE RESPONSE OPERATOR

To estimate the response operator in practice we follow the steps proposed in Appendix A of Falasca (2025) [31]. We report those steps here for completeness.

Given a model $d\mathbf{x} = \mathbf{f}(\mathbf{x})dt + \Sigma d\mathbf{W}$, we build the impulse response operator as follows:

1. We simulate a very long trajectory of the model, starting from a random initial condition and remove an initial transient. We then sample N_e random points from the simulation to define an ensemble of N_e initial conditions on the model's attractor. N_e should be very large (i.e. $N_e \gg 1$) in order to sample the whole attractor and approximate averages over the invariant distribution. Here we chose $N_e = 10^6$ members.
2. For each one of the N_e initial conditions, we impose an impulse perturbation Δ_j to the degree of freedom x_j at time $t = 0$. The amplitude of the perturbation should be theoretically infinitesimally small, ensuring linearity of the response even in nonlinear systems. In practice we do as follows: we consider the long time series of $x_j(t)$ from the long control integration above and define $\Delta_j = 10^{-2}\sigma_j$, where σ_j is the standard deviation of time series $x_j(t)$.
3. Therefore, for a given initial condition $\mathbf{x}(0)$, we simulate two trajectories: a control trajectory without perturbation and a perturbed one, where an impulse perturbation Δ_j has been imposed on the j -th degree of freedom at time $t = 0$. This procedure is repeated in parallel for all initial conditions, resulting in an ensemble of N_e paired of control and perturbed trajectories.

4. At each time t we then estimate the time dependent ensemble average $\langle A(x_k(t)) \rangle$ of an observable $A(x_k(t))$ for both the perturbed and unperturbed run. We refer to the perturbed and control ensemble average respectively as $\langle A(x_k(t)) \rangle_p$ and $\langle A(x_k(t)) \rangle$. The observables considered in this study are going to be: (i) $A(x_k(t)) = x_k(t)$ and (ii) $A(x_k(t)) = (x_k(t) - \mu_k(t))^2$, with $\mu(t)$ representing the time-dependent mean of the distribution, therefore quantifying the response in ensemble mean and variance.

5. We define the impulse response operator for observable $A(x_k(t))$ as

$$R_{k,j}(t) = \frac{\langle A(x_k(t)) \rangle_p - \langle A(x_k(t)) \rangle}{\Delta_j}.$$

VI. NEURAL EMULATORS OF THE CHARNEY-DEVORE MODEL: STATIONARY STATISTICS

Stationary density and autocorrelation functions of the Charney-deVore system as given by the numerical model, the vanilla emulator and the causal emulator.

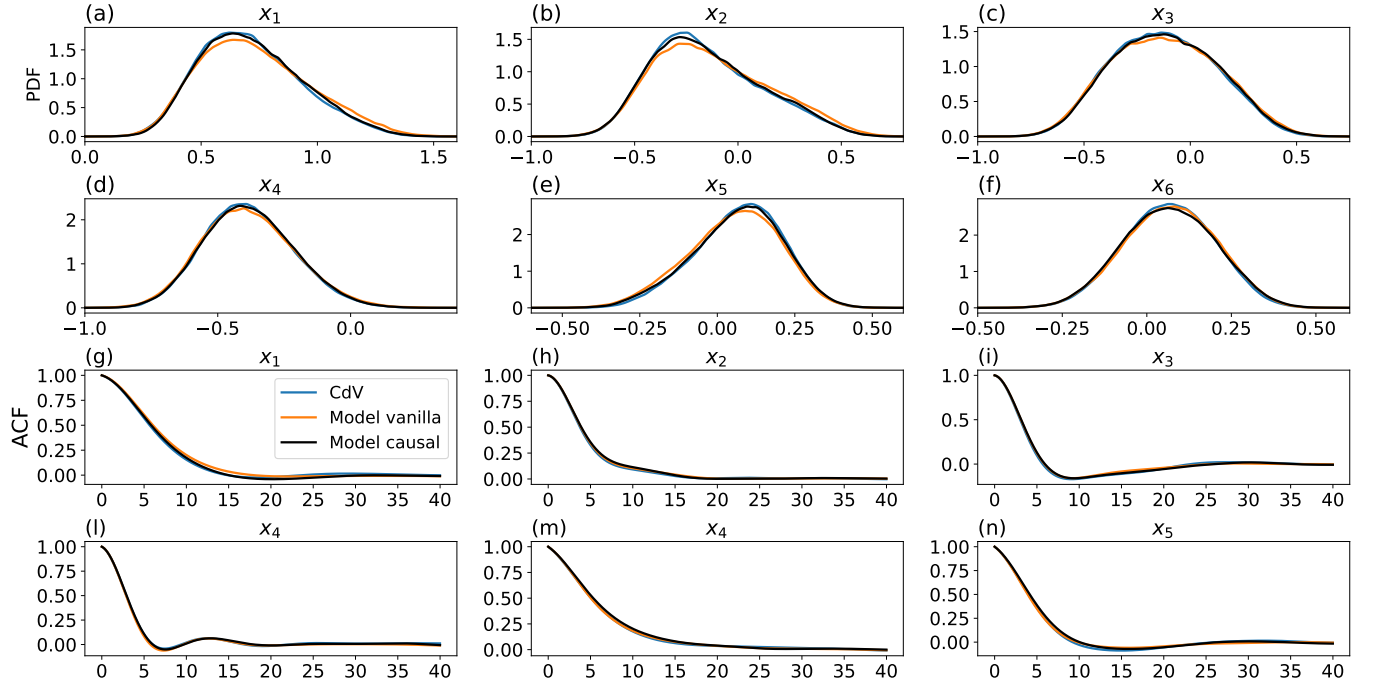


FIG. 3: Stationary statistics. First and second rows: stationary distributions (PDFs) of the variables x_1, \dots, x_6 of the CdV model. Labels: “CdV” refers to the numerical model; “Model vanilla” is the vanilla, unconstrained emulator; “Model causal” is the causally constrained emulator. Third and fourth rows: same as the first row but for the autocorrelation functions (ACFs).

VII. RESPONSE OPERATOR FOR THE CHARNEY-DEVORE MODEL

In Figure 4 and Figure 5, we report the estimation of the full response operator in ensemble mean and variance as obtained by the numerical model and the two emulators. The response operators have been computed with the method presented in Section V and using $N_e = 10^6$ ensemble members. The unconstrained, vanilla emulator provides a very good representation of responses to impulse perturbations, as expected given the large training dataset and Markovianity of the system [31]. The causally constrained emulator yields a systematically improved representation of both mean and variance responses. This is further quantified by the total time-dependent MSE, aggregated over all j and k , between the emulators and the ground truth. This analysis is shown in Figure 6.

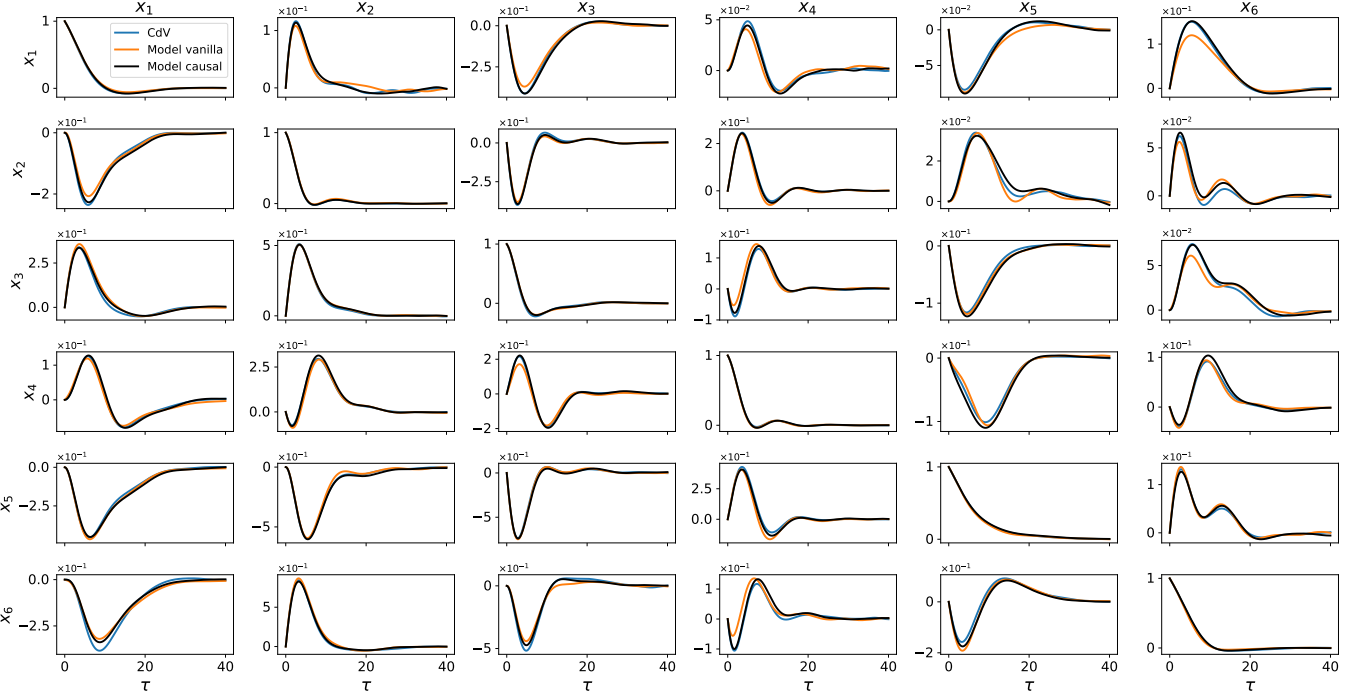


FIG. 4: Time-dependent, responses in ensemble mean of variable $x_k(t)$ to an impulse perturbation the CdV model in Eq. (3) in the main text as predicted by the unconstrained and causally constrained emulators. Example: column (1), row (2) represents what is the time-dependent response of $x_{k=2}(t)$ given a small, impulse perturbation imposed on $x_{j=1}(0)$ at time $t = 0$. Labels: “CdV” refers to the numerical model; “Model vanilla” is the vanilla, unconstrained emulator; “Model causal” is the causally constrained emulator.

VIII. RESPONSE TO LARGE STEP FUNCTION FORCINGS IN THE CHARNEY-DEVORE MODEL

We now consider the nonlinear response regime by adding a step function forcing \mathbf{F} to both the numerical (CdV) and neural models. In the main text we focused on the case $\dot{\mathbf{x}} = \mathbf{F} + \mathbf{f}(\mathbf{x}) + \Sigma \xi(t)$, where $\mathbf{F} = (\sigma_1, 0, 0, 0, 0, 0)$ for $t \geq 0$, σ_1 being the std. dev. of the x_1 variable. We stress that this is a very large forcing, imposed on a model that had only access to unperturbed variability. Here, we perform six forcing experiments, applying a step forcing to each degree of freedom in turn with amplitude equal to its standard deviation: $\mathbf{F} = (\sigma_1, 0, \dots, 0)$, $(0, \sigma_2, 0, \dots, 0)$, \dots , $(0, \dots, 0, \sigma_6)$. For each case, we analyze the time-dependent response of the ensemble mean and variance of the full system. Results are shown in Fig. 7 (mean) and Fig. 8 (variance). The causally coarse-grained emulator outperforms the unconstrained, vanilla emulator. Notably, the vanilla emulator becomes unstable in three out of six forcing experiments (rows 1, 2, and 6 in Fig. 7), whereas the causally constrained emulator remains stable in all cases. Errors in the ensemble-mean response are primarily observed when the step forcing is applied to x_5 and x_6 . To elucidate the origin of these errors, we revisit the response operator $R_{k,j}(t)$ inferred in the previous sections and focus on the ground-truth response estimated from the numerical model. We quantify the cumulative sensitivity of the system to perturbations applied to each degree of freedom x_j as $D_j = \sum_{t=0}^{\tau_\infty} \sum_k R_{k,j}(t)$, where $\tau_\infty = 40$ Model Time Units, consistent with all response analyses. The resulting sensitivities are shown in Fig. 9. This analysis identifies x_5 and x_6 as the most sensitive degrees of freedom: perturbations applied to these variables induce the largest cumulative system-wide response. This high sensitivity provides a plausible, qualitative explanation for the observed degradation in ensemble-mean responses under large forcings applied to x_5 and x_6 , where even small modeling errors are strongly amplified.

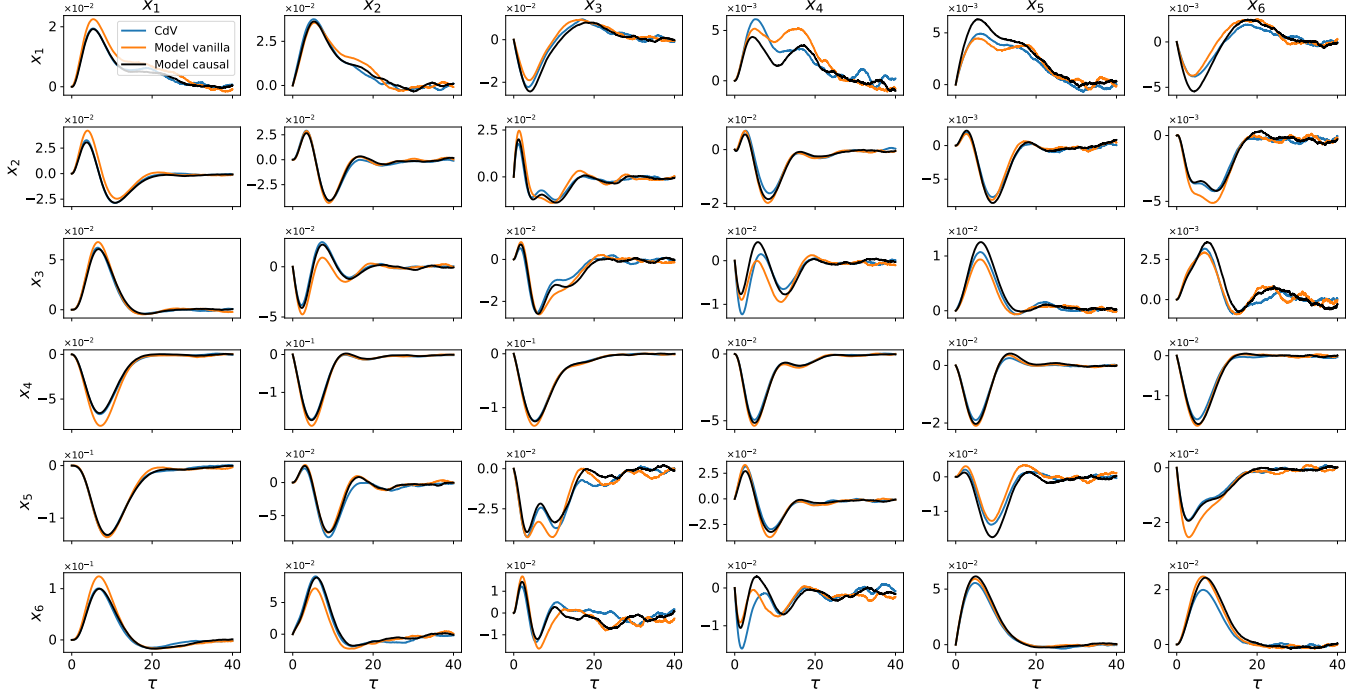


FIG. 5: Time-dependent, responses in ensemble variance of variable $x_k(t)$ to an impulse perturbation the CdV model in Eq. (3) in the main text as predicted by the unconstrained and causally constrained emulators. Example: column (1), row (2) represents what is the time-dependent response of $x_{k=2}(t)$ given a small, impulse perturbation imposed on $x_{j=1}(0)$ at time $t = 0$. Labels: “CdV” refers to the numerical model; “Model vanilla” is the vanilla, unconstrained emulator; “Model causal” is the causally constrained emulator.

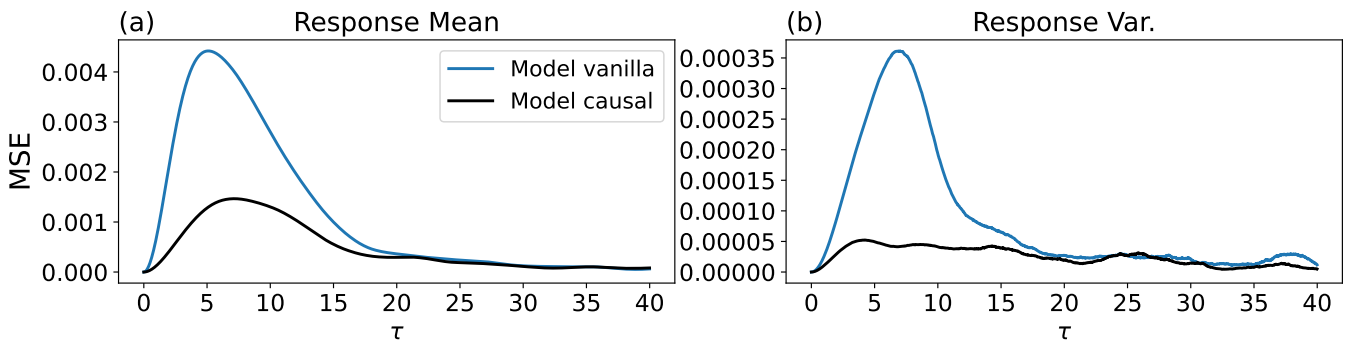


FIG. 6: Perturbed statistics in the linear regime. Panel (a): Total MSE over time for the mean response, computed from the full response operator $\mathbf{R}(t) \in \mathbb{R}^{6,6}$ for each model. Panel (b): Same as Panel (a) but the response in ensemble variance.

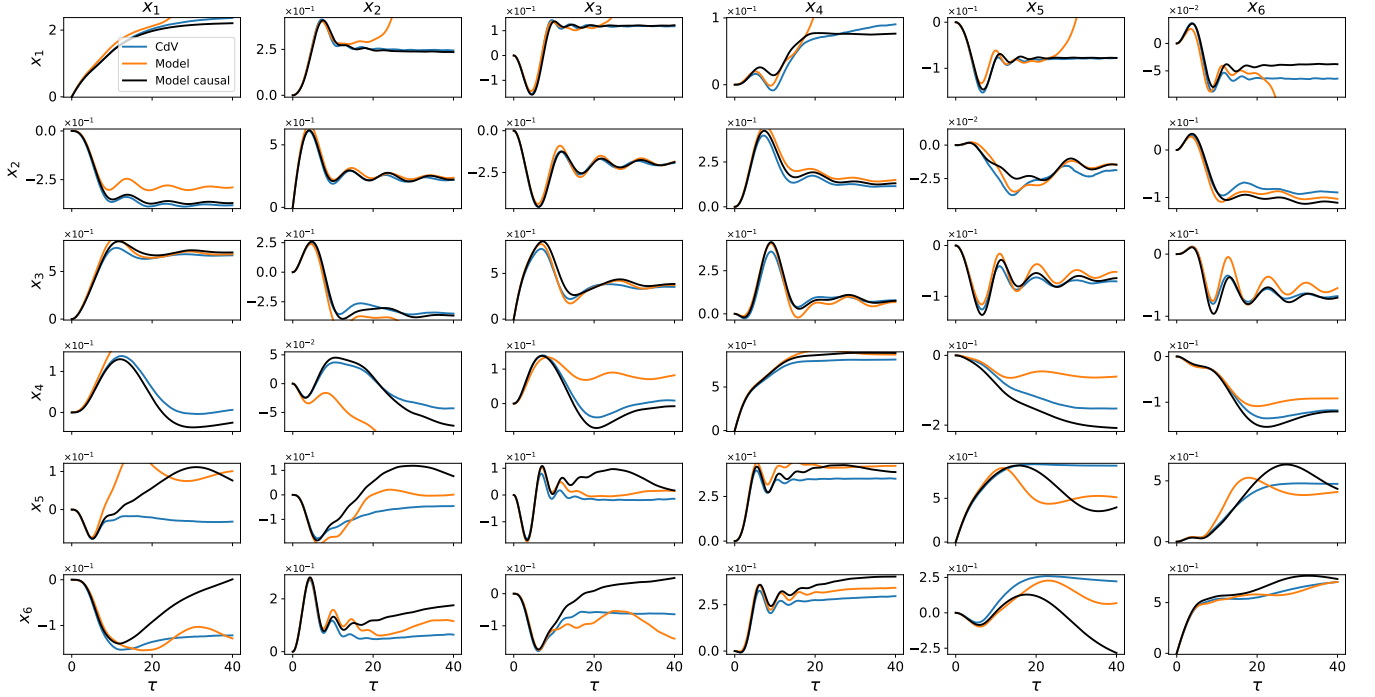


FIG. 7: Perturbed statistics in the nonlinear regime. Row (i) shows the response in ensemble mean to a step function forcing applied on x_i ; e.g. Row (1): response in ensemble mean response a step function forcing $\mathbf{F} = (\sigma_1, 0, 0, 0, 0, 0)$ applied for $t \geq 0$, where σ_1 is the standard deviation of x_1 . Row (2): same as Row (1) but using $\mathbf{F} = (0, \sigma_2, 0, 0, 0, 0)$. Labels: “CdV” refers to the numerical model; “Model vanilla” is the vanilla, unconstrained emulator; “Model causal” is the causally constrained emulator.

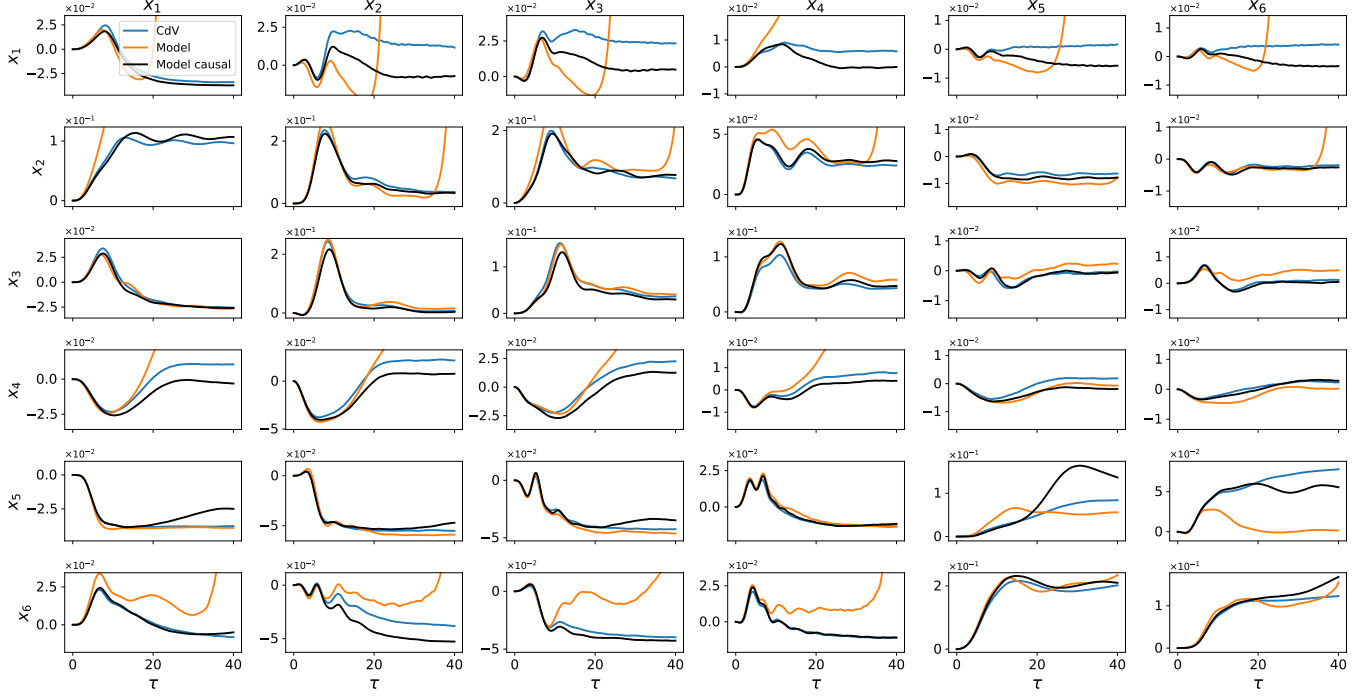


FIG. 8: Perturbed statistics in the nonlinear regime. Row (i) shows the response in ensemble variance to a step function forcing applied on x_i ; e.g. Row (1): response in ensemble mean to a step function forcing $\mathbf{F} = (\sigma_1, 0, 0, 0, 0, 0)$ applied for $t \geq 0$, where σ_1 is the standard deviation of x_1 . Row (2): same as Row (1) but using $\mathbf{F} = (0, \sigma_2, 0, 0, 0, 0)$. Responses are computed using an ensemble of $N_e = 10^5$ members. Labels: “CdV” refers to the numerical model; “Model vanilla” is the vanilla, unconstrained emulator; “Model causal” is the causally constrained emulator.

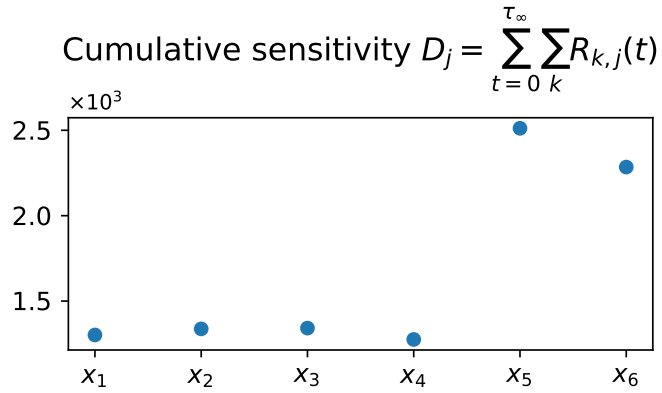


FIG. 9: Cumulative (causal) sensitivity $D_j = \sum_{t=0}^{\tau_\infty} \sum_k R_{k,j}(t)$ of the Charney-DeVore model in Eq. (3) in the main text. For the response operator $R_{k,j}(t)$ we use the correct ground-truth. The system is more sensitive to perturbations on degrees of freedom x_5 and x_6 , therefore providing a possible explanation for the degradation of results when adding large, step function forcings on these degrees of freedoms.